The synaptonemal complex assembles between meiotic chromosomes by wetting

Spencer G. Gordon[1], Chiu Fan Lee[2], Ofer Rog[1,*]

[1]School of Biological Sciences and Center for Cell and Genome Sciences, University of Utah, United States;
[2]Department of Bioengineering, Imperial College London, United Kingdom
* correspondence: ofer.rog@utah.edu

Summary

Exchange of genetic information between the parental chromosomes during sexual reproduction is controlled by a conserved structure called the synaptonemal complex. It is composed of axes (stiff chromosomal backbones), and a central region that assembles between two parallel axes. To form exchanges, the parental chromosomes must be drawn together and aligned by the synaptonemal complex. However, its mechanism of assembly remains unknown. Here we identify an axis-central region interface in *C. elegans* composed of the axis component HIM-3 and the central region component SYP-5. Weaker interface prevented complete synaptonemal complex assembly, and crucially, altered its canonical layered ultrastructure. Informed by these phenotypes, we built a thermodynamic model for synaptonemal complex assembly. The model recapitulates our experimental observations, indicating that the liquid-like central region can move chromosomes by wetting the axes without active energy consumption. More broadly, our data show that condensation can bring about tightly regulated nuclear reorganization.

Keywords

synaptonemal complex, meiosis, *C. elegans*, condensation, wetting, HORMA

Introduction

Cellular processes are tightly controlled spatially, requiring that large structures, such as organelles or chromosomes, be moved and precisely positioned. This is most commonly achieved by motor proteins and the polymerization/depolymerization of cytoskeletal filaments. These active processes consume free energy provided by the hydrolysis of nucleotide triphosphate (NTP) molecules to move cargo over large distances. However, an alternative mechanism that could regulate cellular organization has been proposed: thermodynamically-driven formation of protein assemblies (Brangwynne *et al.* 2009). Self-assembly of biomolecular condensates is capable of exerting pico-newton-scale forces on adjacent cellular bodies (Gouveia *et al.* 2022). However, the importance of condensate assembly for driving and controlling the movement of cellular structures *in vivo* remains unknown.

A cellular structure whose maneuvering is particularly well-regulated is the chromosome. During meiosis, the specialized cell division cycle that produces gametes, the unassociated homologous parental chromosomes (homologs) are brought together and aligned along their lengths (Zickler and Kleckner 2023). Paired and aligned homologs are necessary for the formation of exchanges (crossovers) that shuffle the maternal and paternal genomes and allow chromosomes to correctly segregate into the gametes. Errors in these intricately controlled processes lead to aneuploidy, congenital birth defects and infertility.

Chromosome alignment in meiosis is driven and controlled by the synaptonemal complex – a conserved protein structure that assembles between homologs. The structure is built from two main elements – axes and the synaptonemal complex central region (SC-CR; Figure 1A-B). The axes are composed of cohesins, HORMA-domain proteins and other structural and regulatory proteins, which mold the chromosome into an array of loops. The SC-CR, made of coiled-coil proteins, associates with pre-assembled axes on each of the two homologs, placing them parallel to one another and ~150nm apart. Synaptonemal complex assembly, or synapsis, extends localized pairing interactions to align the homologs end-to-end and intimately juxtapose homologous sequences. The synaptonemal complex also directly regulates factors that form crossover (Libuda *et al.* 2013), potentially by regulating their diffusion along chromosomes (Morgan *et al.* 2021; Zhang *et al.* 2021; Durand *et al.* 2022; Fozard *et al.* 2023).

The mechanism of synaptonemal complex assembly remains unknown. The ladder-like appearance of the SC-CR in negative-stained electron micrographs (Figure 1A), the stereotypic organization of subunits within the SC-CR (Figure 1B; (Schild-Prüfert *et al.* 2011; Schücker *et al.* 2015; Köhler *et al.* 2020)), and its assembly through processive extension (Rog and Dernburg 2015; Pollard *et al.* 2023) all contributed to the idea that assembly proceeds through zipping. This mode of assembly would be similar to active polymerization - locally consuming free energy generated by NTP hydrolysis to attach subunits at the growing end and in this way resist the restoring force of chromatin. The more recent observations of constant SC-CR subunit exchange within the synaptonemal complex and of fluid behaviors exhibited by the SC-CR suggest that it is a biomolecular condensate with liquid properties (Rog *et al.* 2017; Pattabiraman *et al.* 2017; Nadarajan *et al.* 2017; von Diezmann *et al.* 2024). The synaptonemal complex may therefore assemble by condensation of the SC-CR between parallel axes, moving chromosomes by capillary-like forces. However, available tools to reconstitute, perturb, and image the synaptonemal complex have failed to distinguish between possible assembly mechanisms. Underlying these challenges is the inability to modulate the interactions between the SC-CR and the axis, since the molecular contacts between them are not known (Gordon and Rog 2023).

Here, we identify components of the axis-SC-CR interface in the nematode *Caenorhabditis elegans*, comprising the axis protein HIM-3 and the SC-CR protein SYP-5. We show that this interface is essential for synaptonemal complex assembly. Moreover, the effects of weakened axis-SC-CR interactions on the morphology of the synaptonemal complex support SC-CR assembly through wetting. To substantiate this idea, we generated a thermodynamic model. Our model assumes no local consumption of free energy and relies on the condensation of SC-CR molecules and on surface binding of SC-CR components to the axis to account for the experimentally observed phenotypes of meiotic perturbations.

Results

The axis protein HIM-3 is a component of the axis-SC-CR interface

To identify the axis-SC-CR interface, we wanted to study this interface independently of other mechanisms that affect chromosome organization. We used polycomplexes: assemblies of SC-CR material that form when the SC-CR cannot load onto chromosomes. Since the stacked SC-CR lamellae in polycomplexes closely resemble the SC-CR layer that forms between the axes under physiological conditions, polycomplexes have been used to study SC-CR ultrastructure (Sym and Roeder 1995; Hughes and Hawley 2020). We used worms that lack meiotic cohesins (deletion of the meiotic kleisins *rec-8* and *coh-3/4*, designated *cohesin(-)*), which prevents axis assembly onto chromosomes. In these worms, SC-CR material

forms chromatin-free polycomplexes that recruit axis components (Figures 1A, 1C and S1B; (Severson and Meyer 2014; Rog *et al.* 2017)).

First, we wanted to identify the axis components required for polycomplex-axis interactions. Out of the four meiotic HORMA proteins in worms - HTP-3, HIM-3 and HTP-1/2 - we predicted a crucial role for HIM-3 based on its proximity to the SC-CR and the increasing synapsis defects upon its gradual removal (Kim *et al.* 2015; Köhler *et al.* 2017; Gordon and Rog 2023). Upon deletion of *him-3*, the axis components HTP-3 and HTP-1/2 failed to localize to polycomplexes, as revealed by immunostaining (Figure 1C-D). This suggested that HIM-3 directly interacts with the SC-CR, whereas HTP-3 and HTP-1/2 are recruited to polycomplexes indirectly, through interactions with HIM-3 (Kim *et al.* 2014). Sequential deletions of HIM-3 regions showed that the C-terminus of HIM-3, which includes a disordered linker and a domain that interacts with other HORMA proteins (called the 'closure motif'), plays only a minimal role in the recruitment of axis proteins to polycomplexes (Figure 1C-D). This result suggested that the SC-CR-interacting region lies in the HORMA domain of HIM-3.

The HORMA domain is a conserved fold shared among meiotic axis proteins (Ur and Corbett 2021). We examined the structures of the HORMA domains in the three meiotic axis proteins (Figure 2A; (Kim *et al.* 2014)) to identify divergent surfaces that could mediate HIM-3's specific contribution to axis-SC-CR interactions. We noticed a positively charged patch that is unique to HIM-3, containing lysines at positions 170, 171, 177 and 178 and an arginine at position 174 (Figure 2A). Importantly, this patch is in a region of HIM-3 not known to carry out other functions, like interaction with other axis proteins (Figure S2A; (Kim *et al.* 2014)). We generated several HIM-3 mutants that reversed the charge in the positive patch (Figure 2A). These mutations decreased the accumulation of HIM-3 on polycomplexes: ~4-fold for *him-3*^{R174E} and reduction to almost background level for *him-3*$^{KK170\text{-}171EE}$ and *him-3*$^{KK177\text{-}178EE}$ (Figure 2B-E; in panel E we normalized HIM-3 enrichment relative to SYP-5 enrichment). The indirect recruitment of HTP-3 to polycomplexes was also abolished. Analysis in live *cohesin(-)* gonads, using GFP-tagged HIM-3, yielded similar results (Figure S3; ~5-fold reduction for *him-3*^{R174E} versus wild-type worms). These data indicate that the positive patch on HIM-3 mediates association with SC-CR components.

The HIM-3 positive patch is essential for synaptonemal complex assembly

To assess the contribution of the HIM-3 positive patch to synapsis, we analyzed meiosis in our HIM-3 positive patch mutants. Worms harboring *him-3*^{R174E} and *him-3*$^{KK170\text{-}171EE}$ exhibited disrupted meiosis, consistent with their relative disruption of axis-SC-CR interactions. The *him-3*^{R174E} worms had only 21 progeny on average, as compared with 300 progeny for wild-type worms, with 4.2% male self-progeny, indicative of mis-segregation of the *X* chromosome (Figure 3A-B; wild-type worms have 0.1% male progeny). These defects were much more severe in *him-3*$^{KK170\text{-}171EE}$ worms, which exhibited phenotypes similar to *him-3* null worms (Couteau *et al.* 2004) and were almost sterile.

Cytological examination indicated that an average of 3.2 out of the six chromosome pairs synapsed in *him-3*^{R174E} worms, and only 1.5 chromosomes synapsed in *him-3*$^{KK170\text{-}171EE}$ worms (Figure 3C-D and S4A). The synapsed chromosomes appear to form crossovers, as indicated by the correspondence between the number of synapsed chromosomes and the number of chromosomes attached through chiasmata (Figure 3E). The residual association of SC-CR material with axes in *him-3*$^{KK170\text{-}171EE}$ worms suggests that other axis

components may harbor a weak affinity for the SC-CR. Consistent with this idea, chromosomes with axes that lack HIM-3 altogether are still associated with SC-CR material (Figure 3F; (Kim *et al.* 2014)).

Importantly, HIM-3 positive patch mutant proteins still loaded onto both synapsed and asynapsed chromosomes (Figure 3C). HIM-3 levels and the fraction of HIM-3 on chromosomes were also minimally affected in the mutants (Figure S4B-D). These data suggest that the surface charge alterations in *him-3* are *bona fide* separation-of-function mutations, and that the phenotypes they exhibit can be attributed to disrupted axis-SC-CR interactions.

Disrupting axis-SC-CR interactions alters synaptonemal complex morphology

To gain better insight into the morphology of the synaptonemal complex in *him-3* mutants, we used stimulated emission-depletion super-resolution microscopy (STED). The axes in wild-type worms, and in most synapsed chromosomes in *him-3*^{R174E} worms, exhibited the canonical layered ultrastructure of an assembled synaptonemal complex: they were parallel along their length, separated by ~150nm (Figure 3F-H; (Page and Hawley 2004; Almanzar *et al.* 2023; Zickler and Kleckner 2023)). *him-3*$^{KK170\text{-}171EE}$ and *him-3(-)* chromosomes, however, were much more disorganized. Axes were often associated with each other without being parallel and even seemingly aligned axes failed to maintain a 150nm spacing (Figure 3G). In some cases, SC-CR aggregates interacted with multiple axes - a situation never observed in wild-type worms (Figure 3F-G).

Staining a protein that localizes in the middle of the SC-CR (SYP-2; Figure 1B; (Schild-Prüfert *et al.* 2011; Köhler *et al.* 2020)) revealed that many of the SC-CR structures in *him-3*$^{KK170\text{-}171EE}$ worms do not form the single thread observed in wild-type animals, implying the inter-axes space is occupied by more than a single lamella of SC-CR (Figure 3F). Instead, the SYP-2 epitope exhibited a dotty appearance with some parallel threads (Figures 3F and S5). Measurements in live worms confirmed the presence of many more SC-CR molecules per chromosome in *him-3*$^{KK170\text{-}171EE}$ worms compared with wild-type or *him-3*^{R174E} worms (Figure S10F). This pattern is reminiscent of polycomplexes, which resemble stacked SC-CR lamellae, with a distance between the center of each lamella (where SYP-2 localizes) matching the width of native synaptonemal complex (Figure S5; (Rog *et al.* 2017; Hughes and Hawley 2020)).

Taken together, our analyses indicate that HIM-3-mediated axis-SC-CR interactions drive synaptonemal complex assembly. Furthermore, the altered SC-CR morphology in *him-3* mutants sheds light on the mechanism of synapsis, pointing to an interplay between axis-SC-CR interactions and self-interactions among SC-CR subunits. Below, we use this understanding to generate a thermodynamic model for synaptonemal complex assembly.

The SC-CR protein SYP-5 is a component of the axis-SC-CR interface

To identify SC-CR components that interact with the HIM-3 positive patch, we searched the worm SC-CR subunits - SYP-1-6 and SKR-1/2 - to identify those that harbor negatively charged regions that localize near the axes. An attractive candidate was SYP-5, which has a negatively charged C-terminus that localizes near the axes and, when truncated, leads to synapsis defects (Figure 1B; (Hurlock *et al.* 2020; Zhang *et al.* 2020). (The C-terminus of SYP-1, which also localizes near the axes, is not negatively charged.)

We generated two charge-swap mutants in *syp-5* (*syp-5*^{5K} and *syp-5*^{6K}, mutating five and six aspartic and glutamic acids to lysines, respectively; Figure 4A). We analyzed them in the *cohesin(-) him-3*$^{KK170\text{-}171EE}$ background, hypothesizing they may restore the recruitment of axis components to polycomplexes. We found that polycomplexes in *cohesin(-) him-3*$^{KK170\text{-}171EE}$ *syp-5*^{5K} worms recruited significantly more HIM-3 compared to *cohesin(-) him-3*$^{KK170\text{-}171EE}$ controls (Figure 4B-E). This likely underestimates the effect of *syp-5*^{5K} on axis-SC-CR interactions, since polycomplexes in this background concentrated much less SC-CR, likely due to impaired SC-CR self-interactions (Figures 4C and S10B; (Zhang *et al.* 2020)). The *syp-5*^{6K} mutation further weakened SC-CR self-interactions, completely preventing polycomplex formation in *cohesin(-) him-3*$^{KK170\text{-}171EE}$ worms and precluding assessment of its effect on axis-SC-CR interactions (Figure 4B). These data suggest that the C-terminus of SYP-5 contributes to axis-SC-CR interactions, in addition to promoting self-interactions between SC-CR subunits.

The SYP-5 negatively-charged C-terminus helps maintain synaptonemal complex morphology

When we analyzed *him-3*$^{KK170\text{-}171EE}$ *syp-5*^{5K} and *him-3*$^{KK170\text{-}171EE}$ *syp-5*^{6K} worms, we found only one or two SC-CR-associated chromosomes per nucleus, similar to *him-3*$^{KK170\text{-}171EE}$ worms (Figures 4F-G and S6B). However, the synaptonemal complex on these synapsed chromosomes exhibited morphologies more similar to wild type. This effect was the strongest for *him-3*$^{KK170\text{-}171EE}$ *syp-5*^{6K} worms, where almost all the synaptonemal complexes exhibited a canonical morphology: a single SC-CR thread between the axes and an inter-axis distance of ~150nm (Figure 4H-I).

When analyzed by themselves, both *syp-5*^{5K} and *syp-5*^{6K} worms exhibited defects in synaptonemal complex assembly (Figure S7). These defects included the presence of asynapsed chromosomes and chromosomes that failed to form a crossover, as well as consequent defects in chromosome segregation leading to reduced progeny number and a higher prevalence of male self-progeny (Figure S7). Consistent with its stronger effect on synaptonemal complex morphology in *him-3*$^{KK170\text{-}171EE}$ worms, *syp-5*^{6K} worms exhibited stronger defects compared with *syp-5*^{5K} worms (Figure S7).

While we were unable to generate clean separation-of-function mutations in *syp-5*, the restoration of axis recruitment to polycomplexes and the suppression of the synaptonemal complex morphology defects suggest that the negatively charged C-terminus of SYP-5 interacts with the positively charged patch on HIM-3 to form an axis-SC-CR interface.

Thermodynamic model of synaptonemal complex assembly

Our analysis of *him-3* mutants helps differentiate between different mechanisms of synaptonemal complex assembly. Zipping-based mechanisms predict that disrupting axis-SC-CR interactions will not prevent zipping *per se* but will affect the alignment of the axes (and the chromosomes) by decoupling the axes from the SC-CR. Thermodynamically-driven assembly makes a different prediction. To assemble, condensation mediated by attractive self-interactions and surface binding to the axes overcomes the entropic-driven dispersion of SC-CR components and chromosomes. These interactions together determine the ultimate morphology of the synaptonemal complex. Our observations in *him-3*$^{KK170\text{-}171EE}$ worms support this prediction: the drastically weakened axis-SC-CR interactions led to the formation of a much thicker SC-CR that failed to extend to the entire length of the chromosome (Figures 3 and S12).

To explore whether thermodynamically-driven assembly underlies synapsis, we developed a free-energy-based model. Our model incorporates the dimensions of meiotic nuclei and chromosomes in worms (Figure 5A; see Supplementary Note 1 for a full description of the model). An important quantity in our model is the condensate volume, V_c. We measured V_c for polycomplexes (~0.05 μm^3; Figure 5E) and found it to be somewhat smaller than the volume of the assembled SC-CR on chromosomes (~0.1 μm^3; Figure 5A). That is expected given the affinity between the axes and the SC-CR. Since volume is not easy to measure in fluorescent images, we also used the fraction of SC-CR molecules in condensates (either polycomplexes or assembled synaptonemal complex) as a proxy for V_c (e.g., Figure 5D).

Our model includes energetic terms for two key aspects of synaptonemal complex assembly. The first is the binding of SC-CR molecules to the axis. This depends on the binding energy between SYP-5 (together with other SC-CR components) and HIM-3 (and potentially other axis components), denoted by e_{SH}, as well as the number of interacting axis and SC-CR molecules. Each chromosome harbors a limited number of HIM-3 molecules (~500), which, in turn, allow for ~500 associated SC-CR molecules, each with binding energy e_{SH}. The second free energy component incorporates the interfacial energy between the SC-CR and the nucleoplasm, which depends on attractive binding energy among SYP-5 molecules (and other SC-CR components), denoted by e_{SS}, and on the minimization of the SC-CR–nucleoplasm interfacial area. The morphology of the SC-CR is therefore defined by the balance between the energetic benefit of surface binding to the axes ("adsorption") and the free energy penalty of having a larger surface area for assembled synaptonemal complex threads *versus* a spherical polycomplex. While we cannot directly measure e_{SS} and e_{SH}, our modeling reveals that the effects on synaptonemal complex assembly are best captured by the ratio between these two entities, which we denote as $\alpha = \frac{e_{SH}}{e_{SS}}$.

Synaptonemal complex assembly model recapitulates empirical observations of physiological and perturbed meiosis

The parameterized model captures multiple aspects of wild-type and mutant synapsis. First, we minimized the total free energy in the system when the condensate volume V_c is constant. This resulted in a monotonic relationship between α and the number of synapsed chromosomes (Figure 6A). Using this graph, the six synapsed chromosomes in wild-type worms yield $\alpha > 1.2$. Similarly, the ~3 synapsed chromosomes in *him-3*^{R174E} worms translate to $\alpha = 1.0$. Given the molecular nature of the mutation, this reduction in α likely reflects weaker e_{SH}.

Many of the conditions discussed here affect both α and V_c. To capture these complexities, we plotted the result of the model as a contour plot that links α and V_c to the number of synapsed chromosomes (Figure 6B; note that this plot is a generalization of Figure 6A). The black curves denote the minimal values of α and V_c that would allow the indicated number of chromosomes to synapse. On the contour plot, the wild-type and *him-3*^{R174E} conditions are noted with green and blue asterisks, respectively, and *him-3*$^{KK170\text{-}171EE}$ worms, with an even lower value of α and a somewhat lower V_c (Figures 2 and 5D), is denoted with a red asterisk.

The contour plot also captures information about SC-CR morphology. By integrating the volume of the condensate and the number of synapsed chromosomes, we could deduce the predicted 'thickness' of the SC-CR (i.e., the amount of material packed between the 150nm-spaced axes). Consistent with the large number of SC-CR molecules per chromosome (Figure S10F), the thickness of the SC-CR in *him-3*$^{KK170\text{-}171EE}$

worms is predicted to be >100nm (Figure 6B; thickness thresholds of 90 and 100nm are shown as orange and yellow lines, respectively). Notably, the inter-axes distance in *him-3*$^{KK170\text{-}171EE}$ worms becomes variable and the SC-CR forms structures with ultrastructure related to polycomplexes (Figures 3 and S5; (Rog *et al.* 2017; Hughes and Hawley 2020)). This suggests that only a limited amount of SC-CR material could be sandwiched between the axes while maintaining a native synaptonemal complex morphology; beyond this amount, the SC-CR forms a multi-lamellar structure.

We could similarly overlay on the contour plot the effects of other experimental perturbations. For instance, the *syp-5* mutations that partially suppress the effects of *him-3*$^{KK170\text{-}171EE}$ (Figure 3) represent diagonal upward-left vectors relative to the *him-3*$^{KK170\text{-}171EE}$ single mutant (lower V_c and larger α; black arrow in Figure 6B). This vector would bring the thickness of the condensate below the threshold of multi-lamellar synapsis, consistent with our empirical observations. Similarly, we model the effects of the temperature-sensitive *syp-1*^{K42E} mutation, which destabilizes the SC-CR (Figure S10A; (Gordon *et al.* 2021)), and the impact of lowering the abundance of SC-CR subunits (Figure S11; see Supplementary Note 1 for full details).

Our ability to recapitulate a variety of experimental data using our free-energy-based model indicates that an active mechanism (e.g., polymerization) need not be invoked in the assembly of the synaptonemal complex. Instead, our model indicates that SC-CR wetting of the axes can confer selective assembly of the synaptonemal complex between homologs. We conclude that the dramatic chromosome reorganization necessary for chromosome alignment is driven by a mechanism that does not require any additional energy input beyond thermodynamics.

Discussion

In this study, we identified molecular contacts between the axis and the SC-CR, which allowed us to explore the mechanism of synaptonemal complex assembly. Molecular genetic analysis combined with *in vivo* measurements revealed an electrostatic interface between a positive patch on the HIM-3 HORMA domain and the negatively charged C-terminus of SYP-5. The residual SC-CR-axis association in worms lacking HIM-3 altogether (Figure 3F) suggests that the HIM-3-SYP-5 interaction acts together with additional contacts to form the axis-SC-CR interface.

The rapid sequence divergence of synaptonemal complex components in general, and of SC-CR subunits in particular (Kursel *et al.* 2021), suggest that the molecular details of the HIM-3-SYP-5 interface are likely to be specific to worms. Nevertheless, the axes in most organisms include HORMA domain proteins (Ur and Corbett 2021; Gordon and Rog 2023). Also conserved are the dimensions and ultrastructure of the synaptonemal complex (Page and Hawley 2004; Zickler and Kleckner 2023), and the SC-CR's dynamic behaviors (Rog *et al.* 2017) and its ability to form polycomplexes (Hughes and Hawley 2020). These observations suggest that the mechanism of synaptonemal complex assembly - wetting of axes by the SC-CR - is likely to be conserved as well.

The ability to experimentally modulate the affinity between the SC-CR and the axis allowed us to test mechanisms of synaptonemal complex assembly. The liquid-like properties of the SC-CR, as demonstrated by the dynamic exchange of subunits and an ability to form droplet-like polycomplexes, led us to hypothesize that it assembles by wetting two HIM-3-coated axes. Wetting, which relies on binding (adsorption) to the axes and self-interactions between SC-CR subunits (condensation), allows the

concomitant spread to the entire chromosome and the generation of adhesive forces between the homologous chromosomes. Supporting this idea, a thermodynamic model that assumes only self-interactions between SC-CR subunits and binding interactions between the SC-CR and the axis recapitulated the phenotypes of weakening axis-SC-CR and intra-SC-CR interactions (Figures 5D, 6, S9 and S10) and of lowering SC-CR levels (Figure S11).

Our synaptonemal complex assembly model provides an elegant explanation for the association of SC-CR exclusively with paired axes (MacQueen *et al.* 2005). While the SC-CR has an affinity for the axes, binding to unpaired axes provides a small energetic advantage compared with SC-CR condensation. Stable association with axes only occurs in the context of a fully assembled synaptonemal complex, where SC-CR subunits form a condensate that wets the axes. Weakening SC-CR self-association could expose the tendency of SC-CR molecules to bind unpaired axes. Indeed, two independent SC-CR mutations that weaken intra-SC-CR associations also lead to SC-CR association with unpaired axes (the mutations are the aforementioned *syp-1*^{K42E} and *syp-3(me42)*; Figure S10A; (Smolikov *et al.* 2007; Rog *et al.* 2017; Gordon *et al.* 2021)).

Severe perturbations of axis-SC-CR interactions (*him-3*$^{KK170\text{-}171EE}$ or *him-3(-)*) led to the formation of large SC-CR aggregates within the axes – >400nm between the axes and too far apart to be spanned by a single SC-CR lamella (~150nm; Figure 3F). The potential to form such a structure suggests that the wild-type scenario – where unilamellar SC-CR coats the axes from end to end – reflects a tightly regulated balance between axis-SC-CR binding and the interfacial tension of SC-CR condensates. In addition to enabling end-to-end synapsis of parental chromosomes, such a balance could also counter the thermodynamic drive of liquids to minimize surface tension (e.g., through the process of Ostwald ripening; (Gouveia *et al.* 2022)). Wetting of the axes therefore underlies persistent and complete synapsis – the maintenance of independent SC-CR compartments, one on each chromosome – during the many hours in which the synaptonemal complex remains assembled.

A unilamellar SC-CR has crucial functional implications. Complete synapsis ensures two fundamental characteristics of meiotic crossovers: 1) all chromosomes undergo at least one crossover and 2) crossovers only occur between homologous chromosomes. The specter of multiple axes interacting with large SC-CR aggregates (Figure 3F) is likely to prevent synapsis of all chromosomes by sequestering SC-CR material. It could also allow ectopic exchanges between nonhomologous chromosomes and, consequently, karyotype aberrations and aneuploidy. The limited surface area of a unilamellar SC-CR, together with repulsive forces between chromatin masses (Marko and Siggia 1997), could limit the number of interacting axes to no more than two. Such a mechanism to prevent multi-chromosome associations can help explain the evolutionary conservation of the synaptonemal complex, which exhibits only minor ultrastructural variations between species with order-of-magnitude differences in genome size and chromosome number (Page and Hawley 2004; Zickler and Kleckner 2023).

Our thermodynamic model groups together the distinctive affinities that drive SC-CR self-interactions: stacking of SC-CR subunits and the lateral attachments between SC-CR lamellae. The spherical morphology of stacked ladder-like lamellae in polycomplexes suggests a balance with the anisotropic elements (ladder-like assembly), and the potentially isotropic attractive interactions among SC-CR proteins. This spherical morphology is distinct from mitotic spindles (Oriola *et al.* 2020) but more akin to drops of fragmented amyloid fibrils in yeast (Tyedmers *et al.* 2010). The non-spherical polycomplexes that form in some

organisms (Hughes and Hawley 2020) and in certain mutant backgrounds (e.g., (Gordon *et al.* 2021)) provide an opportunity for future studies of the balance between stacking and lateral interactions.

Cell biologists have identified numerous supramolecular assemblies in the nucleus (Sabari *et al.* 2020). Many of these structures have been suggested to exert force and movement on the genome in order to organize it and thus tightly regulate biological processes ranging from transcription to genome maintenance. The *in vitro* and *in vivo* material properties of many such structures have been a focus of recent probing. However, only rarely has it been shown that a specific material state of a supramolecular assembly (e.g., a liquid) underlies the nuclear-scale maneuvering of chromosomes in the nucleus (Gouveia *et al.* 2022; Chung and Tu 2023). Synaptonemal complex assembly through wetting demonstrates that the liquid properties of the SC-CR underlie a core component of meiosis – the large-scale chromosome reorganization that brings homologous chromosomes together.

Acknowledgments

We would like to thank all members of the Rog lab, Martin Horvath, Yumi Kim, Kevin Corbett and Alyssa Rodriguez for discussions and advice; Amy Strom and Erik Jorgensen for critical reading of this manuscript; Sara Nakielny for editorial work; Maria Diaz de la Loza for scientific illustrations; Yumi Kim and Abby Dernburg for antibodies. Some worm strains were provided by the Caenorhabditis Genetics Center, which is funded by NIH Office of Research Infrastructure Programs (P40 OD010440). We acknowledge the HSC Imaging Core for the use of the STED microscope. Work in the Rog lab is funded by R35GM128804 grant from NIGMS.

Author contributions

SGG carried out all experiments. OR and SGG conceived the project, designed experiments and analyzed data. CFL developed the thermodynamic model. SGG, CFL and OR wrote the paper.

Declaration of interests

The authors declare no competing interests.

Supplemental information

Document S1. Figures S1–S12

Document S2. Supplemental Note 1

Table S1. Excel file containing data related to Model Figure 2A in Supplemental Note 1

Table S2. Excel file containing data related to Model Figure 2B in Supplemental Note 1

Table S3. Excel file containing data related to Model Figure 3 in Supplemental Note 1

Materials and Methods

Worm strains and CRISPR

Worms were grown under standard conditions (Brenner 1974). Unless otherwise noted, all worms were grown at 20°C. All strains used in this study are listed in Table S1. CRISPR was performed as previously described (Gordon *et al.* 2021), with guide RNA and repair templates listed in Table S2. All new alleles were confirmed by Sanger sequencing.

Structural models of HORMA domain-containing proteins

PDB files for HTP-1 and HIM-3 (Kim *et al.* 2014) were obtained from PDB database and uploaded into ChimeraX (Meng *et al.* 2023). Electrostatic models of surface charge were created with the Surfaces tab on ChimeraX. Models of *him-3* charge swap mutants were created using the Rotamers tab and changing the specified amino acids to aspartic acid residues with the 'best predicted' position. The HORMA domain of HTP-3 was generated in AlphaFold (Senior *et al.* 2020) without the C-terminal tail. The best-predicted structure was used.

Immunofluorescence and fluorescence measurements on polycomplexes

Immunofluorescence was performed as described in (Gordon *et al.* 2021). Images were acquired with a Zeiss LSM880 microscope equipped with an AiryScan and a x63 1.4NA Oil objective. The laser powers were kept the same at 1.5% 633nm, 0.3% 561nm, 2.2% 488nm and 4.5% 405nm. The antibodies used were guinea pig anti-HTP-3 (MacQueen *et al.* 2005), rabbit anti-SYP-5 (Hurlock *et al.* 2020), chicken anti-HIM-3 (Hurlock *et al.* 2020), and rabbit anti-SYP-2 (Colaiácovo *et al.* 2003), with appropriate secondary antibodies (Jackson ImmunoResearch). Line scans were analyzed in ZEN Blue 3.0 (Zeiss) on a single z-slice where the polycomplex has the highest fluorescence. The average fluorescence inside the polycomplex and in the nucleoplasm (outside the polycomplex) were used to determine enrichment on polycomplexes. To normalize, the enrichment of the axis component was divided by the enrichment of the SC-CR component.

Meiotic phenotypes

Progeny and male counts were performed as in (Gordon *et al.* 2021). Synapsed chromosomes were counted in maximum-intensity projection images of gonads stained for an SC-CR component (SYP-2 or SYP-5). Chiasmata were counted as in (Gordon *et al.* 2021). Synapsis phenotypes were determined on STED images and were confirmed with line scans to determine that the inter-axis distance was greater than 150nm.

STED imaging

Immunofluorescence slides were made as above, with the following modifications. We used rabbit anti-SYP-5 (Hurlock *et al.* 2020), rabbit anti-SYP-2 (Hurlock *et al.* 2020) and guinea pig anti-HTP-3 primary antibodies, and STAR RED anti-rabbit (Abberoir; 1:200) and Alexa fluor 594 anti-guinea pig (Jackson ImmunoResearch; 1:200) as secondary antibodies. We used liquid mount (Abberoir) as a mounting media. Imaging on STEDYCON was done as in (Almanzar *et al.* 2023). Line scans were used to determine the distance between axes, as described in (Almanzar *et al.* 2023).

Live gonad imaging

Live imaging of gonads was performed essentially as described in (von Diezmann and Rog 2021). Briefly, 2% agarose pads soaked with embryonic culture medium (ECM; 84% Leibowitz L-15 without phenol red, 9.3%

fetal bovine serum, 0.01% levamisole and 2 mM EGTA) for ~20 minutes. Worms were dissected in 20µL ECM supplemented with Hoechst 33342 (1:200). The slides were sealed with VALAP and imaged using 4% 488 laser power 4.5% 405 laser power. Images were processed using Imaris 10.0 (Bitplane). 5 nuclei from each gonad were cropped and a mask for the 488 channel was made. The mask was applied using the default setting, but was manually adjusted as appropriate, particularly in some genotypes (*syp-3* RNAi and *htp-3(-)*).

RNAi

RNAi was performed as described in (Libuda *et al.* 2013). Briefly, *syp-3* (F39H2.4) and RNAi control (pL4440) plasmids from the Ahringer laboratory RNAi library (Kamath *et al.* 2003) were grown overnight in LB+carbenicillin at 37°C, spread on RNAi plates (NGM+carbenicillin+IPTG) and incubated overnight at 37°C. L4 worms were placed on RNAi plates and grown for 24 hours at 20°C. Live gonads were imaged as described above.

CRISPR

CRISPR/Cas9 injections were performed essentially as described in (Gordon *et al.* 2021), with the templates and guides listed in Table S1. Correct repair was confirmed by Sanger sequencing.

Statistical analysis

All statistical analysis was done in Prism 10.0 (GraphPad).

Table S1: Strains used in this work

genotype	source/method
gfp::him-3 IV	(Stauffer *et al.* 2019)
gfp::him-3 rec-8(slc38)/nT1 IV; coh-4(tm1857) coh-3(gk112) V/nT1 [qIs51] V	mating of *gfp::him-3* with *coh-3 coh-4/nT1*, followed by CRISPR to create *rec-8(-)*
rec-8(ok978)/nT1 IV; coh-4(tm1857) coh-3(gk112)/nT1 [qIs51] V	(Severson and Meyer 2014)
him-3^{R174E}(slc30) rec-8(ok978)/nT1 IV; coh-4(tm1857) coh-3(gk112)/nT1 [qIs51] V	CRISPR
him-3$^{KK170-171EE}$(slc26) rec-8(ok978)/nT1 IV; coh-4(tm1857) coh-3(gk112)/nT1 [qIs51] V	CRISPR
him-3$^{KK177-178EE}$(slc28) rec-8(ok978)/nT1 IV; coh-4(tm1857) coh-3(gk112)/nT1 [qIs51] V	CRISPR
gfp::him-3^{R174E}(slc30)/nT1 IV	CRISPR
gfp::him-3$^{KK170-171EE}$(slc29)/nT1 IV	CRISPR
syp-5^{5K}(slc33)II; him-3$^{KK170-171EE}$(slc26) rec-8(ok978)/nT1 IV; coh-4(tm1857) coh-3(gk112)/nT1 [qIs51] V	CRISPR
syp-5^{6K}(slc36) II; him-3$^{KK170-171EE}$(slc26) rec-8(ok978)/nT1 IV; coh-4(tm1857) coh-3(gk112)/nT1 [qIs51] V	CRISPR
syp-5^{5K}(slc33) II; gfp::him-3$^{KK170-171EE}$(slc29)/nT1 IV; +/nT1 [qIs51] V	CRISPR
syp-5^{6K}(slc36) II; gfp::him-3$^{KK170-171EE}$(slc29)/nT1 IV; +/nT1 [qIs51] V	CRISPR
syp-3(ok758) I; ieSi11[gfp::syp-3] II	(Rog and Dernburg 2015)
him-3$^{\Delta 43}$(slc39) rec-8(ok978)/nT1 IV; coh-4(tm1857) coh-3(gk112) /nT1 [qIs51] V	CRISPR
gfp::him-3^{R174E}(slc30) rec-8(slc38)/nT1 IV; coh-4(tm1857) coh-3(gk112)/nT1 [qIs51] V	CRISPR
gfp::him-3$^{KK170-171EE}$(slc29) rec-8(slc38)/nT1 IV; coh-4(tm1857) coh-3(gk112)/nT1 [qIs51] V	CRISPR
syp-3(ok758) htp-3(tm3655)/hT2 [qIS48] (I,III); ieSi11[gfp::syp-3] II	mating
syp-3(ok758) htp-3(tm3655)/hT2 [qIS48] (I,III); ieSi11[gfp::syp -3] syp-5^{5K}(slc33) II	CRISPR
syp-5^{5K}(slc33) II	CRISPR
syp-5^{6K}(slc36) II	CRISPR
syp-3(ok758) I; ieSi11[gfp::syp-3] II ; him-3^{R174E} (slc30)/nT1 IV; +/nT1 [qIs51] V	CRISPR
syp-3(ok758) I; ieSi11[gfp::syp-3] II ; him-3$^{KK170-171EE}$ (slc29)/nT1; +/nT1 [qIs51] V	CRISPR

Table S2: Details on CRISPR-generated alleles

mutation	guide	repair template (guide is underlined)	genotyping primers	genotyping restriction enzyme
him-3^{R174E}	GCACAATC AAGAAACT TCAC (CGG)	ATACCGACAACACGAAACAAATGTT TGCAAGCACAATCAAGAAGCTTCAC GAATGTATCAAGAAAATGGAGCCGC TTCCTCAAGGGTCCG	OR818/ OR819	eliminating AgeI and a.a. changing mutations in red generating HindIII in green
him-3$^{KK170-171EE}$	GCACAATC AAGAAACT TCAC (CGG)	ATACCGACAACACGAAACAAATGTT TGCAAGTACTATCGAAGAGCTTCAT CGATGTATCAAGAAAATGGAGCCGC TTCCTCAAGGGTCCG	OR818/ OR819	eliminating AgeI in red creating ScaI in green creating ClaI in red a.a. changing mutations in blue
him-3$^{KK177-178EE}$	GCACAATC AAGAAACT TCAC (CGG)	CACGAAACAAATGTTTGCAAGCACA ATCAAGAAACTTCATCGATGTATCG AAGAGATGGAGCCGCTTCCTCAAGG GTCCGACGCG	OR818/ OR819	eliminating AgeI and generating ClaI in red a.a. changing mutations in blue
him-3$^{\Delta 43}$	CTTGAAGC AAGACTTC GATC (TGG)	TTCAAATGCTTGCTGCTTCACAATA CTTGAAGCAAGACTTCTAACGGCC-- ATAAAACGACCACACTCAATCCAAA TATGTCA	OR818/ OR819	generating HaeIII in green creating stop codon in blue deleting PAM site in red
him-3(-) (premature stop; novel null allele)	GAAATTCC TATAGCCA GCCAG (TG G)	TGAGCACCGCGAGTCTGAAATTCCT ATAGCTAGCCAGTGAAAGGCCACGT TTCCCGTTGATCTAGAGATTGAAAA AAATT	OR795/ OR796	generating NheI in green creating stop codon and eliminating PAM in blue
syp-5^{5K}	atttcagG ATCTGAAC GACG (AGG)	aaaaaatttcagGATCTGAACAAAA AGAAGGGTAAAGCGAAACAAAGCAT ATGGGGAAGCGACGATTAGaaacga ttatt	OR837/ OR839	generating NdeI in green a.a. changing mutations in blue
syp-5^{6K}	GAGCCAAA TCAAAGGA TGAC (AGG)	CCGAACAGAGCCAAATCAAAGAAGA AGAGAAAAAGTAAGAAAAGTAAAAA GgtAagCtttatattaatttttta atcga	OR837/ OR839	generating HindIII in green a.a. changing mutations in blue
rec-8(-) (premature stop; novel null allele)	AAAAGATG CCGTGTTT CACG (TGG)	TGGTTGTCTCTGCGGAAGTAATTCG ATAGGATTGAGTG- TTCACGGGCCTTGgtgagttttctc atcttttcaatc	OR890/ OR892	generating HindIII in green a.a. changing mutations in blue

Figure 1

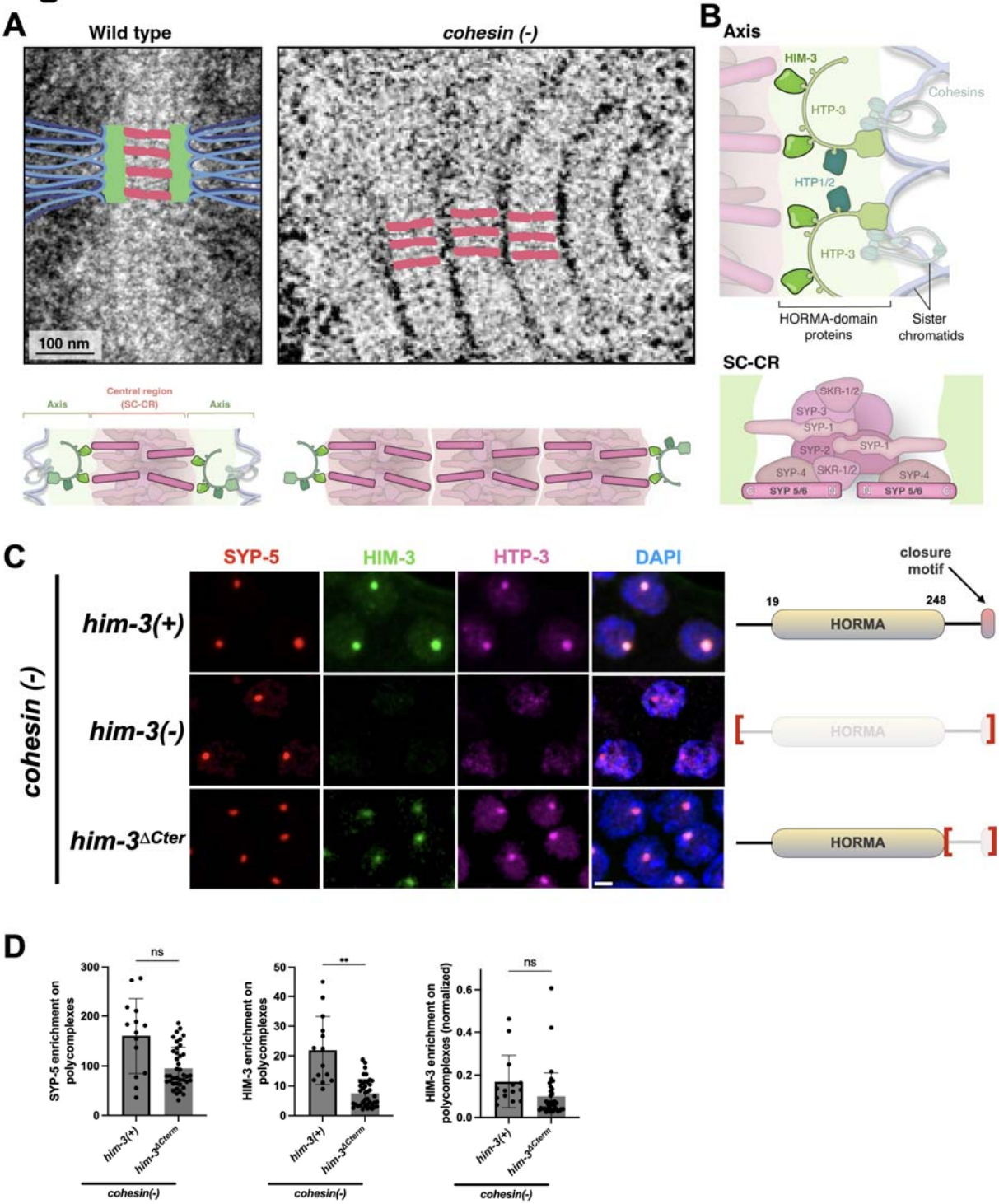

455
456

Figure 1: The HORMA domain of HIM-3 is required for axis interactions with the SC-CR

(A) Top left, assembled synaptonemal complex with the darkly-stained parental chromosomes to its side (left) and of the polycomplexes that form in *cohesin(-)* worms (right) as seen in negative negative-stain electron-micrographs (adapted from (Rog *et al.* 2017)). Bottom left, interpretive diagrams colored magenta for the SC-CR, green for the axes (also called lateral or axial elements) and blue for chromatin. (B) Models depicting the worm components of the axis (top) and the SC-CR (bottom). The position of each of these components within the synaptonemal complex is based on (Köhler *et al.* 2017, 2020; Hurlock *et al.* 2020; Zhang *et al.* 2020; Blundon *et al.* 2024). The pairs HTP-1/2, SYP-5/6 and SKR-1/2 are each partially redundant with each other. (C) Pachytene nuclei from worms of the indicated genotypes stained for the SC-CR component SYP-5 (red) and the axis components HIM-3 (green) and HTP-3 (magenta). The merged images on the right also show DNA (DAPI, blue). The HTP-3 antibody weakly cross-reacts with the nucleolus. Scale bar = 1 µm. Gene models of HIM-3, with the HORMA domain and the closure motif highlighted, are shown to the right. Regions deleted are denoted by red brackets. See Figure S1A for images of the gonads. (D) Quantification of the images in panel A. The enrichment at polycomplexes relative to the nucleoplasm was done using line scans. Normalized HTP-3 enrichment was calculated by dividing HTP-3 enrichment by SYP-5 enrichment.

Figure 2

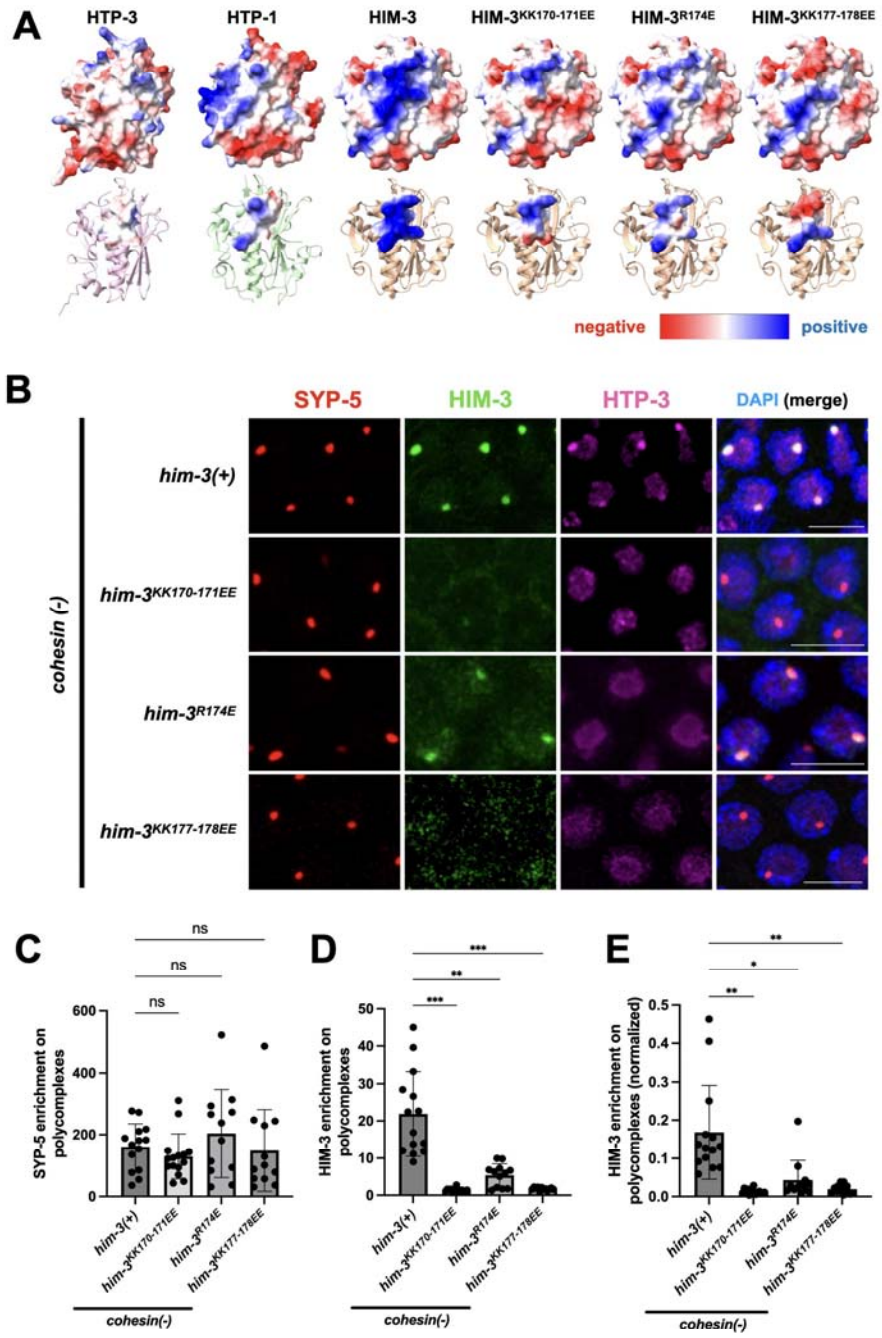

475
476

Figure 2: Axis interactions with the SC-CR are mediated by a positive patch on the HORMA domain of HIM-3

(A) Structural models of the meiotic HORMA proteins, with surface charge plotted in a red-blue scale. The structures of HTP-1 and HIM-3 are from (Kim *et al.* 2014). The models of HTP-3 and the three HIM-3 mutants were generated in AlphaFold (Senior *et al.* 2020). Bottom, secondary structural models, with amino acids constituting the positive patch on HIM-3 (positions 170, 171, 174, 177 and 178), and the analogous positions in HTP-1 and HTP-3 are shown as surfaces colored according to charge. (B) Pachytene nuclei from worms of the indicated genotypes stained for the SC-CR component SYP-5 (red) and the axis components HIM-3 (green) and HTP-3 (magenta). The merged images on the right also show DNA (DAPI, blue). The HTP-3 antibody weakly cross-reacts with the nucleolus. Scale bars = 1 µm. See Figure S2B for images of the gonads and Figure S3 for similar analysis in live gonads. (C-E) Quantification of the images in panel B. The enrichment at polycomplexes relative to the nucleoplasm was done using line scans. Normalized enrichment (panel E) was calculated by dividing HIM-3 enrichment by SYP-5 enrichment.

Figure 3

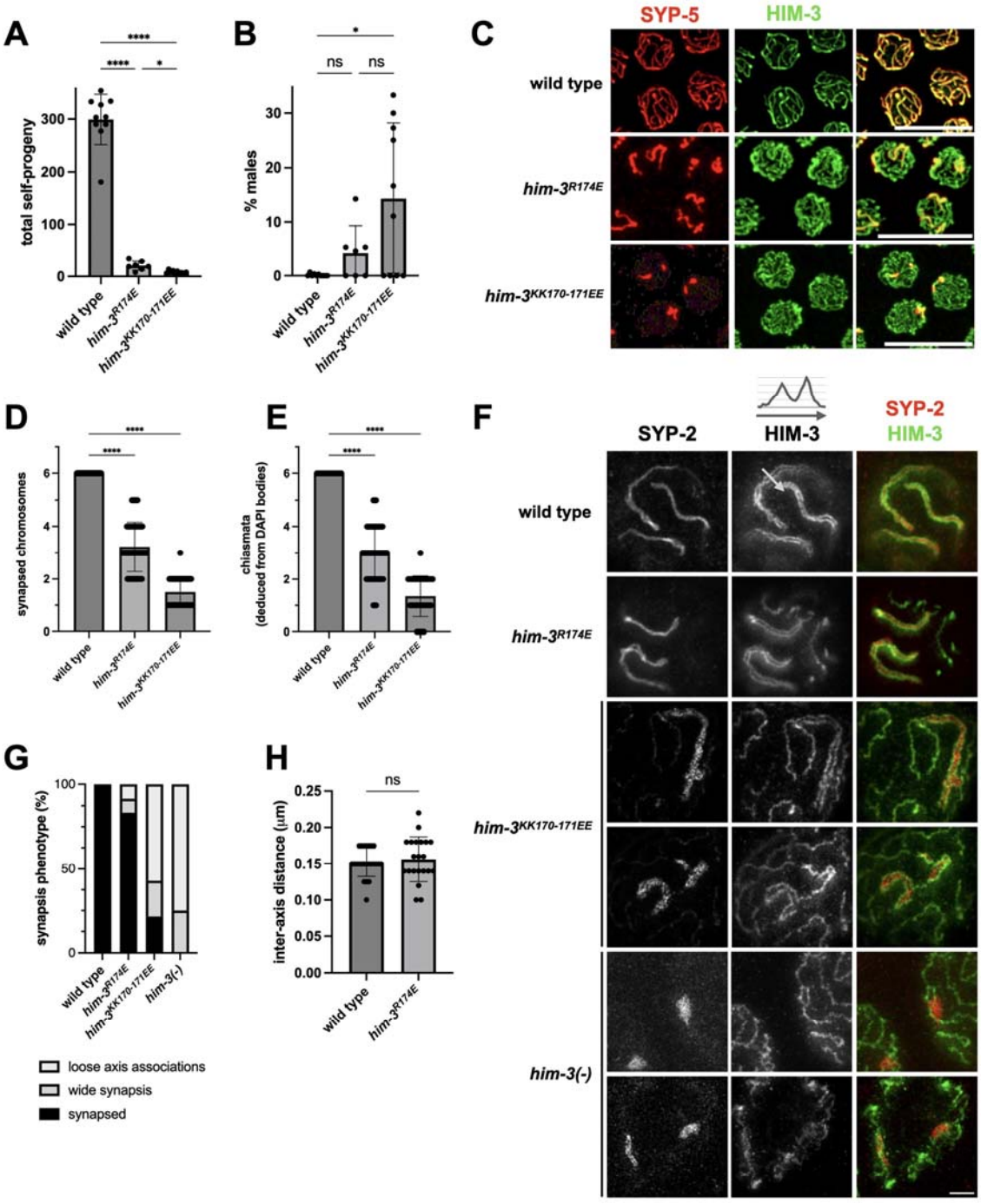

Figure 3: Lowering SC-CR affinity for the axes perturbs synapsis

(A) Total self-progeny from hermaphrodites of the indicated genotypes. (B) Percentage of males among self-progeny of hermaphrodites of the indicated genotypes, indicative of meiotic *X* chromosome non-disjunction. (C) Pachytene nuclei stained for the SC-CR component SYP-5 (red) and the axis component HIM-3 (green), with merged images shown on the right. Note the extensive asynapsis in the *him-3* mutants (i.e., axes lacking SC-CR staining) despite loading of the mutated HIM-3 proteins onto the axis. Scale bars = 10 µm. See Figure S4A for images of the gonads. (D) Quantification of the images in panel C, indicating a smaller number of synapsed chromosomes in *him-3* mutants. (E) Chiasmata number deduced from the number of DAPI bodies at diakinesis. Wild-type animals undergo one chiasma per chromosome, for a total of six chiasmata per nucleus. (F) STED microscopy images of pachytene nuclei stained for the SC-CR component SYP-2 (red in the merged image) and the axis component HIM-3 (green in the merged image). An example of a line scan through a synapsed chromosome is shown above the HIM-3 staining in wild-type animals. Scale bar = 1 µm. (G) Quantification of different synapsis phenotypes in STED images, as shown in panel (F). 'Wide synapsis' indicates parallel axes separated by more than 150nm, as shown in the top nucleus from *him-3*$^{KK170\text{-}171EE}$ animals. 'Loose axis associations' indicate axes wrapped around SC-CR structures, as shown in the bottom nucleus from *him-3*$^{KK170\text{-}171EE}$ animals. (H) Inter-axes distance in the indicated genotypes, measured from nuclei stained as in panel F. Distance was measured only between parallel axes that had unilamellar SYP-2 staining.

Figure 4

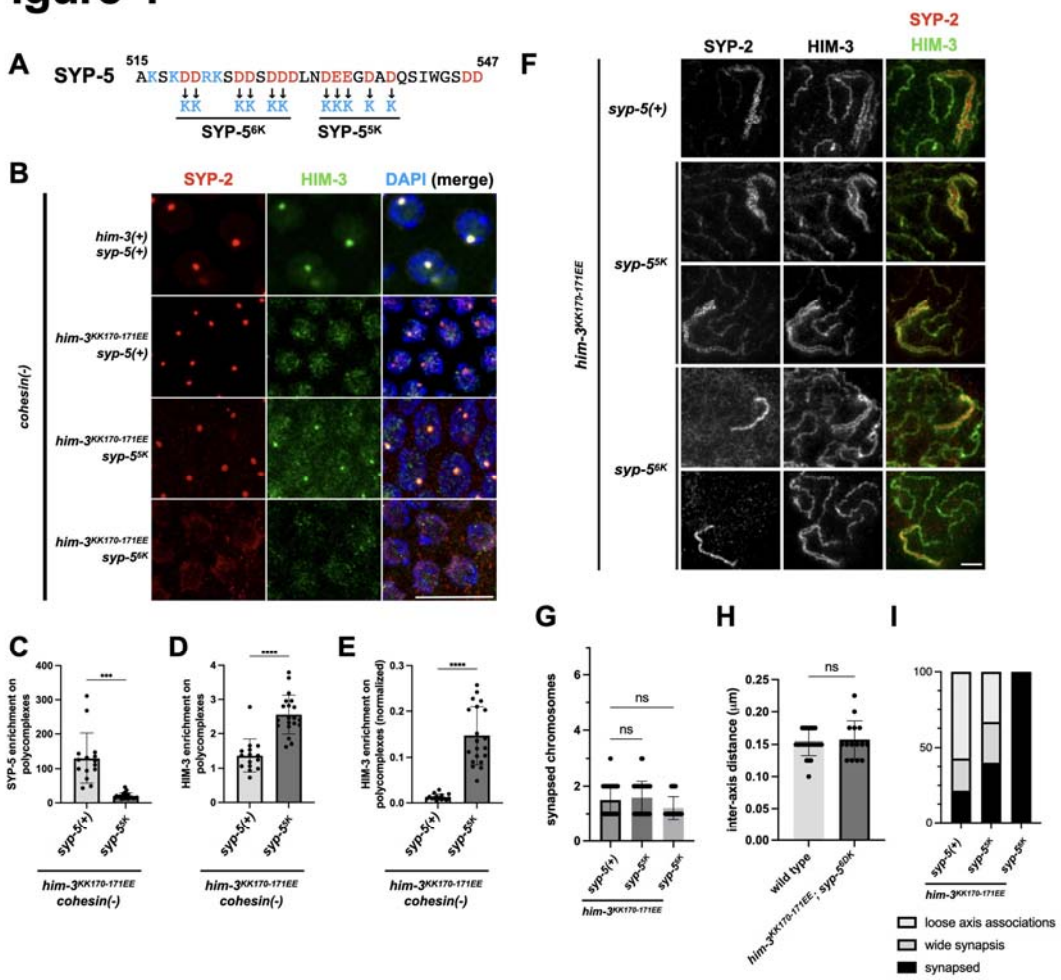

Figure 4: The C-terminus of SYP-5 contributes to SC-CR interactions with the axis

(A) The C-terminus of SYP-5 (amino acids 515-547), with positively- and negatively-charged residues colored in blue and red, respectively. Below, *syp-5* mutations flipping charges in the C-terminus. (B) Pachytene nuclei of the indicated genotypes stained for the SC-CR component SYP-2 (red) and the axis component HIM-3 (green). The merged images on the right also show DNA (DAPI, blue). Note that the *syp-5*^{6K} mutant fails to form polycomplexes, likely due to perturbed self-interactions of the SC-CR. Scale bars = 10 µm. See Figure S6A for images of the gonads. (C-E) Quantification of the enrichment of SYP-2 and HIM-3 to polycomplexes. While the SC-CR is less enriched at polycomplexes in *syp-5*^{5K} animals, these polycomplexes recruit more HIM-3. In panel E, HIM-3 enrichment is normalized to the level of SYP-2 enrichment. (F) STED microscopy images of pachytene nuclei stained for the SC-CR component SYP-2 (red in the merged image) and the axis component HIM-3 (green in the merged image). Scale bar = 1 µm. (G) The number of SC-CR structures per pachytene nuclei in the indicated genotypes. (H) Inter-axes distance in the indicated genotypes, measured from nuclei stained as in panel F. Distance was measured only for *him-3*$^{KK170-171EE}$ *syp-5*^{6K} mutants, where the parallel axes exhibited unilamellar SC-CR staining, and is compared to the data from Figure 3H. (I) Quantification of different synapsis phenotypes in STED images, as shown in panel F. See Figure 3G for more details.

Figure 5

A

	value	reference
nuclear volume	22.5μm^3	nuclear radius = 1.75μm
nucleplasm volume	9.2μm^3	nucleolar radius = 1μm ~50% chromatin-occupied
axis length	72μm	12 chromosomes chromosome length = 6μm
SC-CR length	36μm	6 chromosome pairs
SC-CR width	100nm	(Goldstein and Slaton, 1982)
'ladder rungs' spacing	24.2nm	Panel B
SC-CR thickness	35nm	(Köhler et al., 2017, 2020)
total chromatin loop number	1,375	(Woglar et al., 2020) genome size: 220 Mb loop size: 160 kb
total HIM-3 molecules	11,000	(Woglar et al., 2020) HIM-3 molecules per loop: 8
total SYP-3 molecules	9,200	Panel C
chromosome-associated SYP-3	82%	Panel D
polycomplex volume	0.05μm^3	Panel E
SC-CR volume	0.1μm^3	6x6μmx100nmx35nm

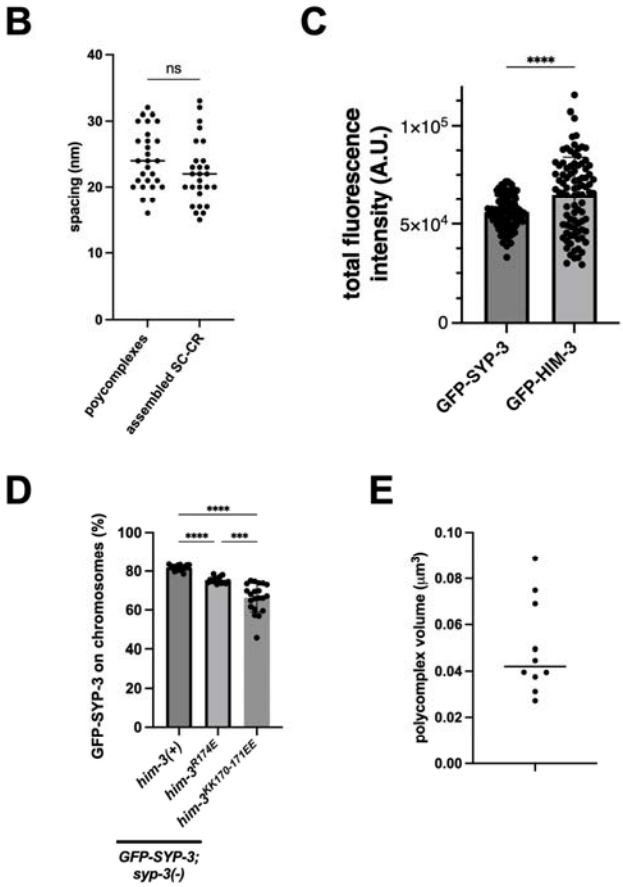

Figure 5: Parameters for the thermodynamic model of synaptonemal complex assembly

(A) Parameters used to model synaptonemal complex assembly. Sources: (Goldstein and Slaton 1982; Köhler *et al.* 2017, 2020; Woglar *et al.* 2020). (B) Distance between the 'ladder rungs' in negative stain electron microscopy images from (Rog *et al.* 2017). Each point represents an individual measurement between adjacent 'rungs'. (C) Total nuclear fluorescence of GFP-HIM-3 and GFP-SYP-3 in pachytene nuclei, yielding a ratio of 1:1.2 GFP-SYP-3 to GFP-HIM-3. (D) The fraction of GFP-SYP-3 on chromosomes in animals of the indicated genotypes is significantly lower in *him-3*^{R174E} and *him-3*$^{KK170\text{-}171EE}$ mutants. (E) Polycomplex volume calculated based on the dimensions of polycomplexes in negative stain electron microscopy images from (Rog *et al.* 2017). Given the mostly spherical appearance of polycomplexes, the z-dimension is assumed to be the average of the widths and height. Each point indicates a single polycomplex.

Figure 6

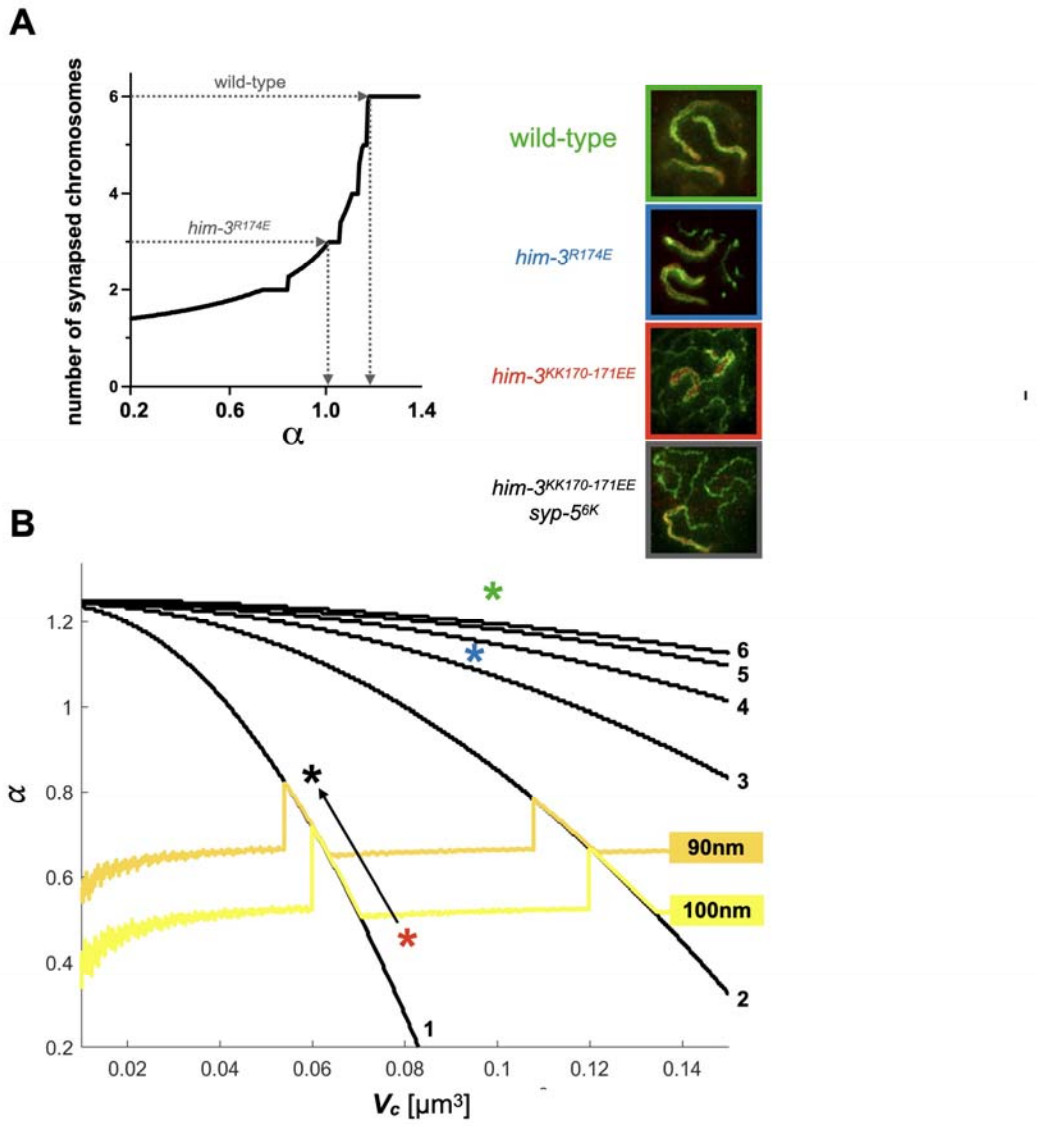

Figure 6: Results of the thermodynamic model of synaptonemal complex assembly

(A) Predicted number of synapsed chromosomes as a function of $\alpha = \frac{e_{SH}}{e_{SS}}$. The condensate volume is held constant $V_c = 0.1\mu m^3$. Dashed arrows indicate how the number of synapsed chromosomes in wild-type and *him-3*^{R174E} allows to deduce the values of α. (For simplicity, we ignore here the slight reduction [8%] in V_c in *him-3*^{R174E} worms.) (B) Contour plot of the predicted number of synapsed chromosomes (black lines) as a function of V_c and α. The orange and yellow lines indicate threshold SC-CR thickness of 90 and 100nm, respectively. The green, blue and red asterisks denote the position of wild-type, *him-3*^{R174E} and *him-3*$^{KK170-171EE}$ worms, respectively. The black arrow and asterisk indicate the effect of combining the *syp-5* mutations with *him-3*$^{KK170-171EE}$. Top right, example images of the mutations shown on the contour plot, with the axis stained in green and the SC-CR in red. See Supplementary Note 1 for more details.

553 **References**
554

555 Almanzar D. E., S. G. Gordon, C. Bristow, A. Hamrick, L. von Diezmann, *et al.*, 2023 Meiotic DNA exchanges
556 in C. elegans are promoted by proximity to the synaptonemal complex. Life Sci Alliance 6.
557 https://doi.org/10.26508/lsa.202301906

558 Blundon J. M., B. I. Cesar, J. W. Bae, I. Čavka, J. Haversat, *et al.*, 2024 Skp1 proteins are structural
559 components of the synaptonemal complex in C. elegans. Sci Adv 10: eadl4876.

560 Brangwynne C. P., C. R. Eckmann, D. S. Courson, A. Rybarska, C. Hoege, *et al.*, 2009 Germline P granules are
561 liquid droplets that localize by controlled dissolution/condensation. Science 324: 1729–1732.

562 Brenner S., 1974 The genetics of Caenorhabditis elegans. Genetics 77: 71–94.

563 Chung Y.-C., and L.-C. Tu, 2023 Interplay of dynamic genome organization and biomolecular condensates.
564 85: 102252.

565 Colaiácovo M. P., A. J. MacQueen, E. Martinez-Perez, K. McDonald, A. Adamo, *et al.*, 2003 Synaptonemal
566 complex assembly in C. elegans is dispensable for loading strand-exchange proteins but critical for
567 proper completion of recombination. Dev. Cell 5: 463–474.

568 Couteau F., K. Nabeshima, A. Villeneuve, and M. Zetka, 2004 A component of C. elegans meiotic
569 chromosome axes at the interface of homolog alignment, synapsis, nuclear reorganization, and
570 recombination. Curr. Biol. 14: 585–592.

571 Diezmann L. von, and O. Rog, 2021 Single-molecule tracking of chromatin-associated proteins in the C.
572 elegans gonad. J. Phys. Chem. B 125: 6162–6170.

573 Diezmann L. von, C. Bristow, and O. Rog, 2024 Diffusion within the synaptonemal complex can account for
574 signal transduction along meiotic chromosomes. bioRxiv 2024.05.22.595404.

575 Durand S., Q. Lian, J. Jing, M. Ernst, M. Grelon, *et al.*, 2022 Joint control of meiotic crossover patterning by
576 the synaptonemal complex and HEI10 dosage. Nature Communications 13.

577 Fozard J. A., C. Morgan, and M. Howard, 2023 Coarsening dynamics can explain meiotic crossover
578 patterning in both the presence and absence of the synaptonemal complex. Elife 12.
579 https://doi.org/10.7554/eLife.79408

580 Goldstein P., and D. E. Slaton, 1982 The synaptonemal complexes of caenorhabditis elegans: comparison of
581 wild-type and mutant strains and pachytene karyotype analysis of wild-type. Chromosoma 84: 585–
582 597.

583 Gordon S. G., L. E. Kursel, K. Xu, and O. Rog, 2021 Synaptonemal Complex dimerization regulates
584 chromosome alignment and crossover patterning in meiosis. PLoS Genet. 17: e1009205.

Gordon S. G., and O. Rog, 2023 Building the synaptonemal complex: Molecular interactions between the axis and the central region. PLoS Genet. 19: e1010822.

Gouveia B., Y. Kim, J. W. Shaevitz, S. Petry, H. A. Stone, *et al.*, 2022 Capillary forces generated by biomolecular condensates. Nature 609: 255–264.

Hughes S. E., and R. S. Hawley, 2020 Alternative Synaptonemal Complex Structures: Too Much of a Good Thing? Trends Genet. 36: 833–844.

Hurlock M. E., I. Čavka, L. E. Kursel, J. Haversat, M. Wooten, *et al.*, 2020 Identification of novel synaptonemal complex components in C. elegans. J. Cell Biol. 219. https://doi.org/10.1083/jcb.201910043

Kamath R. S., A. G. Fraser, Y. Dong, G. Poulin, R. Durbin, *et al.*, 2003 Systematic functional analysis of the Caenorhabditis elegans genome using RNAi. Nature 421: 231–237.

Kim Y., S. C. Rosenberg, C. L. Kugel, N. Kostow, O. Rog, *et al.*, 2014 The chromosome axis controls meiotic events through a hierarchical assembly of HORMA domain proteins. Dev. Cell 31: 487–502.

Kim Y., N. Kostow, and A. F. Dernburg, 2015 The Chromosome Axis Mediates Feedback Control of CHK-2 to Ensure Crossover Formation in C. elegans. Dev. Cell 35: 247–261.

Köhler S., M. Wojcik, K. Xu, and A. F. Dernburg, 2017 Superresolution microscopy reveals the three-dimensional organization of meiotic chromosome axes in intact Caenorhabditis elegans tissue. Proc. Natl. Acad. Sci. U. S. A. 114: E4734–E4743.

Köhler S., M. Wojcik, K. Xu, and A. F. Dernburg, 2020 The interaction of crossover formation and the dynamic architecture of the synaptonemal complex during meiosis. bioRxiv 2020.02.16.947804.

Kursel L. E., H. D. Cope, and O. Rog, 2021 Unconventional conservation reveals structure-function relationships in the synaptonemal complex. Elife 10. https://doi.org/10.7554/eLife.72061

Libuda D. E., S. Uzawa, B. J. Meyer, and A. M. Villeneuve, 2013 Meiotic chromosome structures constrain and respond to designation of crossover sites. Nature 502: 703–706.

MacQueen A. J., C. M. Phillips, N. Bhalla, P. Weiser, A. M. Villeneuve, *et al.*, 2005 Chromosome sites play dual roles to establish homologous synapsis during meiosis in C. elegans. Cell 123: 1037–1050.

Marko J. F., and E. D. Siggia, 1997 Polymer models of meiotic and mitotic chromosomes. Mol. Biol. Cell 8: 2217–2231.

Meng E. C., T. D. Goddard, E. F. Pettersen, G. S. Couch, Z. J. Pearson, *et al.*, 2023 UCSF ChimeraX: Tools for structure building and analysis. Protein Sci. 32: e4792.

Morgan C., J. A. Fozard, M. Hartley, I. R. Henderson, K. Bomblies, *et al.*, 2021 Diffusion-mediated HEI10 coarsening can explain meiotic crossover positioning in Arabidopsis. Nat. Commun. 12: 4674.

Nadarajan S., T. J. Lambert, E. Altendorfer, J. Gao, M. D. Blower, *et al.*, 2017 Polo-like kinase-dependent phosphorylation of the synaptonemal complex protein SYP-4 regulates double-strand break formation through a negative feedback loop. Elife 6. https://doi.org/10.7554/eLife.23437

Oriola D., F. Jülicher, and J. Brugués, 2020 Active forces shape the metaphase spindle through a mechanical instability. Proceedings of the National Academy of Sciences 117: 16154–16159.

Page S. L., and R. S. Hawley, 2004 The genetics and molecular biology of the synaptonemal complex. Annu. Rev. Cell Dev. Biol. 20: 525–558.

Pattabiraman D., B. Roelens, A. Woglar, and A. M. Villeneuve, 2017 Meiotic recombination modulates the structure and dynamics of the synaptonemal complex during C. elegans meiosis. PLoS Genet. 13: e1006670.

Pollard M. G., B. Rockmill, A. Oke, C. M. Anderson, and J. C. Fung, 2023 Kinetic analysis of synaptonemal complex dynamics during meiosis of yeast Saccharomyces cerevisiae reveals biphasic growth and abortive disassembly. Front Cell Dev Biol 11: 1098468.

Rog O., and A. F. Dernburg, 2015 Direct visualization reveals kinetics of meiotic chromosome synapsis. Cell Rep. 10: 1639–1645.

Rog O., S. Köhler, and A. F. Dernburg, 2017 The synaptonemal complex has liquid crystalline properties and spatially regulates meiotic recombination factors. Elife 6. https://doi.org/10.7554/eLife.21455

Sabari B. R., A. Dall'Agnese, and R. A. Young, 2020 Biomolecular condensates in the nucleus. Trends Biochem. Sci. 45: 961–977.

Schild-Prüfert K., T. T. Saito, S. Smolikov, Y. Gu, M. Hincapie, *et al.*, 2011 Organization of the synaptonemal complex during meiosis in Caenorhabditis elegans. Genetics 189: 411–421.

Schücker K., T. Holm, C. Franke, M. Sauer, and R. Benavente, 2015 Elucidation of synaptonemal complex organization by super-resolution imaging with isotropic resolution. Proc. Natl. Acad. Sci. U. S. A. 112: 2029–2033.

Senior A. W., R. Evans, J. Jumper, J. Kirkpatrick, L. Sifre, *et al.*, 2020 Improved protein structure prediction using potentials from deep learning. Nature 577: 706–710.

Severson A. F., and B. J. Meyer, 2014 Divergent kleisin subunits of cohesin specify mechanisms to tether and release meiotic chromosomes. Elife 3: e03467.

Smolikov S., A. Eizinger, K. Schild-Prufert, A. Hurlburt, K. McDonald, *et al.*, 2007 SYP-3 restricts synaptonemal complex assembly to bridge paired chromosome axes during meiosis in Caenorhabditis elegans. Genetics 176: 2015–2025.

Stauffer W. T., L. Zhang, and A. Dernburg, 2019 Diffusion through a liquid crystalline compartment regulates meiotic recombination, pp. 8–15 in *Biophysics, Biology and Biophotonics IV: the Crossroads*, SPIE.

Sym M., and G. S. Roeder, 1995 Zip1-induced changes in synaptonemal complex structure and polycomplex assembly. J. Cell Biol. 128: 455–466.

Tyedmers J., S. Treusch, J. Dong, J. M. McCaffery, B. Bevis, *et al.*, 2010 Prion induction involves an ancient system for the sequestration of aggregated proteins and heritable changes in prion fragmentation. Proc. Natl. Acad. Sci. U. S. A. 107: 8633–8638.

Ur S. N., and K. D. Corbett, 2021 Architecture and Dynamics of Meiotic Chromosomes. Annu. Rev. Genet. 55: 497–526.

Woglar A., K. Yamaya, B. Roelens, A. Boettiger, S. Köhler, *et al.*, 2020 Quantitative cytogenetics reveals molecular stoichiometry and longitudinal organization of meiotic chromosome axes and loops. PLoS Biol. 18: e3000817.

Zhang Z., S. Xie, R. Wang, S. Guo, Q. Zhao, *et al.*, 2020 Multivalent weak interactions between assembly units drive synaptonemal complex formation. J. Cell Biol. 219. https://doi.org/10.1083/jcb.201910086

Zhang L., W. Stauffer, D. Zwicker, and A. F. Dernburg, 2021 Crossover patterning through kinase-regulated condensation and coarsening of recombination nodules. bioRxiv 2021.08.26.457865.

Zickler D., and N. Kleckner, 2023 Meiosis: Dances Between Homologs. Annu. Rev. Genet. https://doi.org/10.1146/annurev-genet-061323-044915

Figure 1

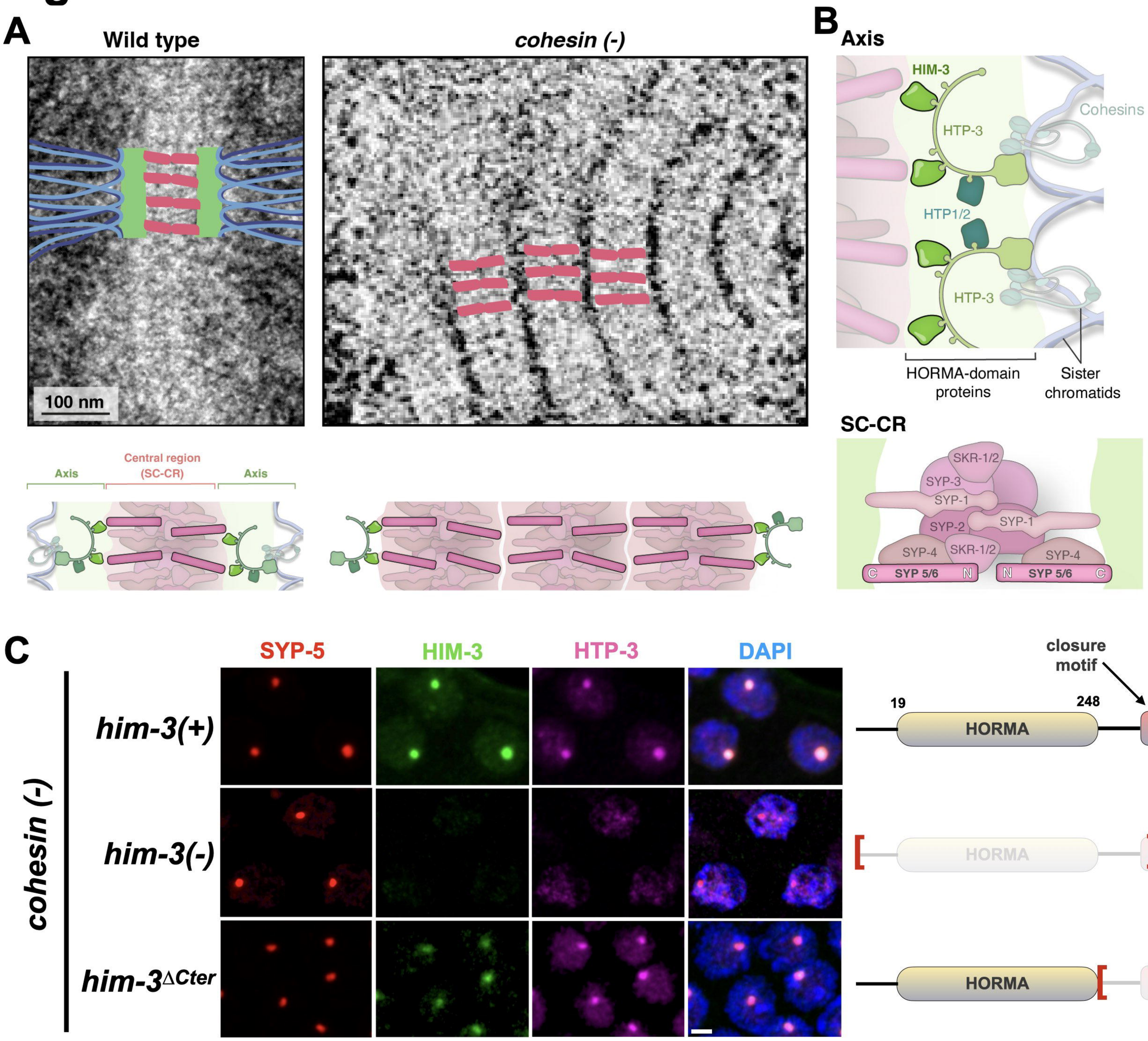

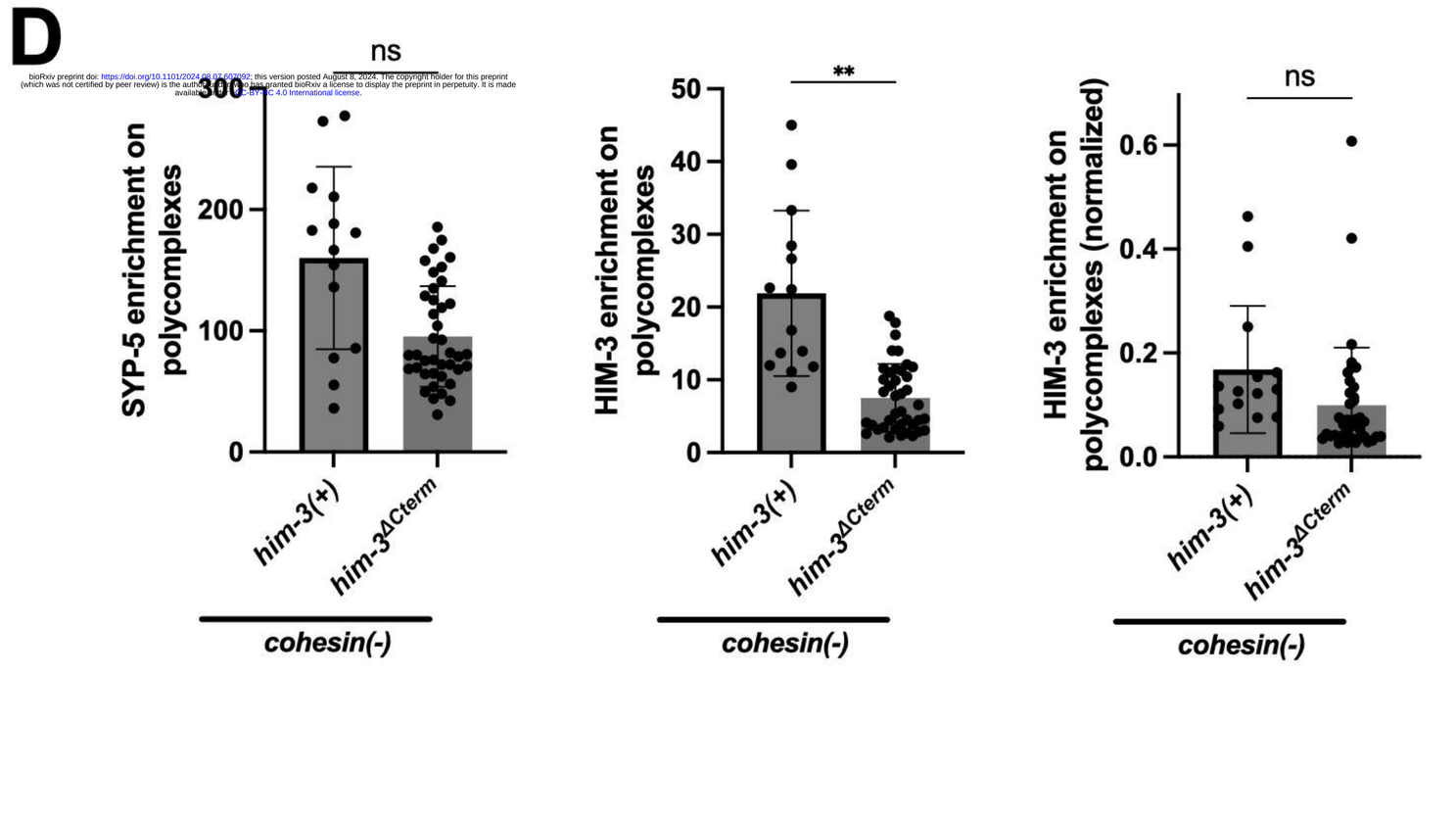

Figure 2

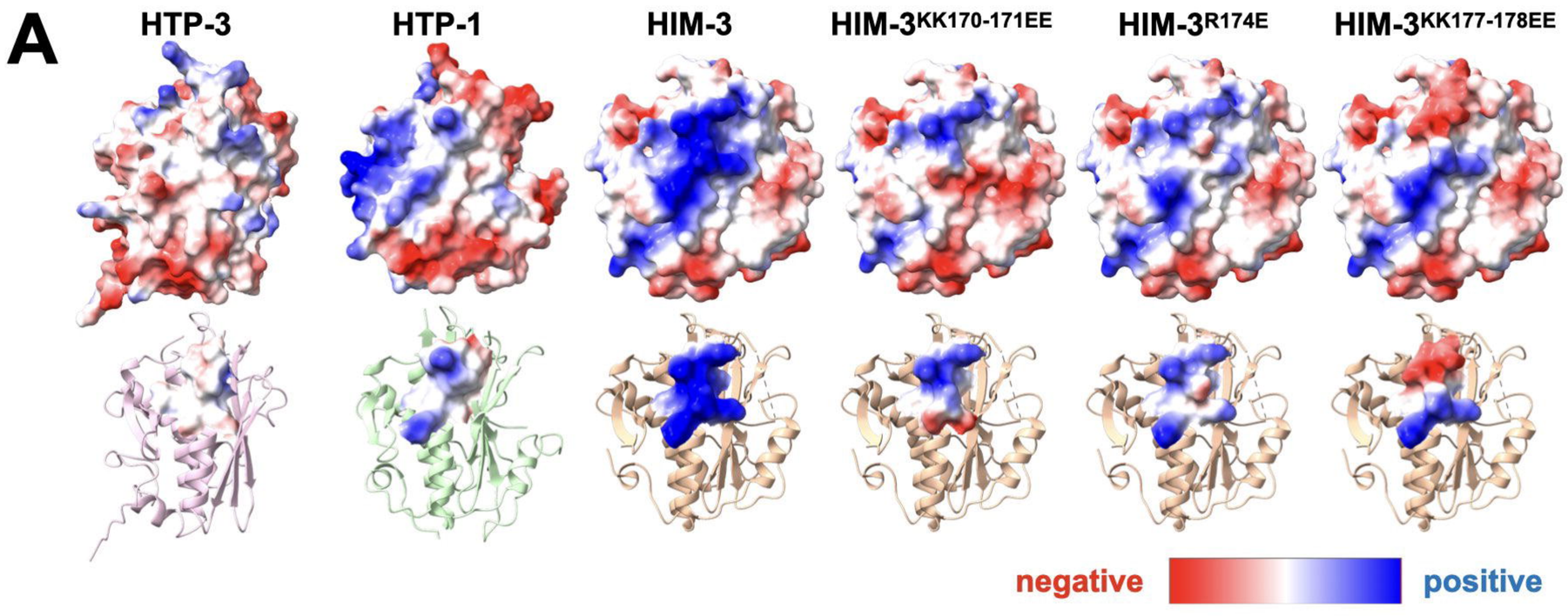

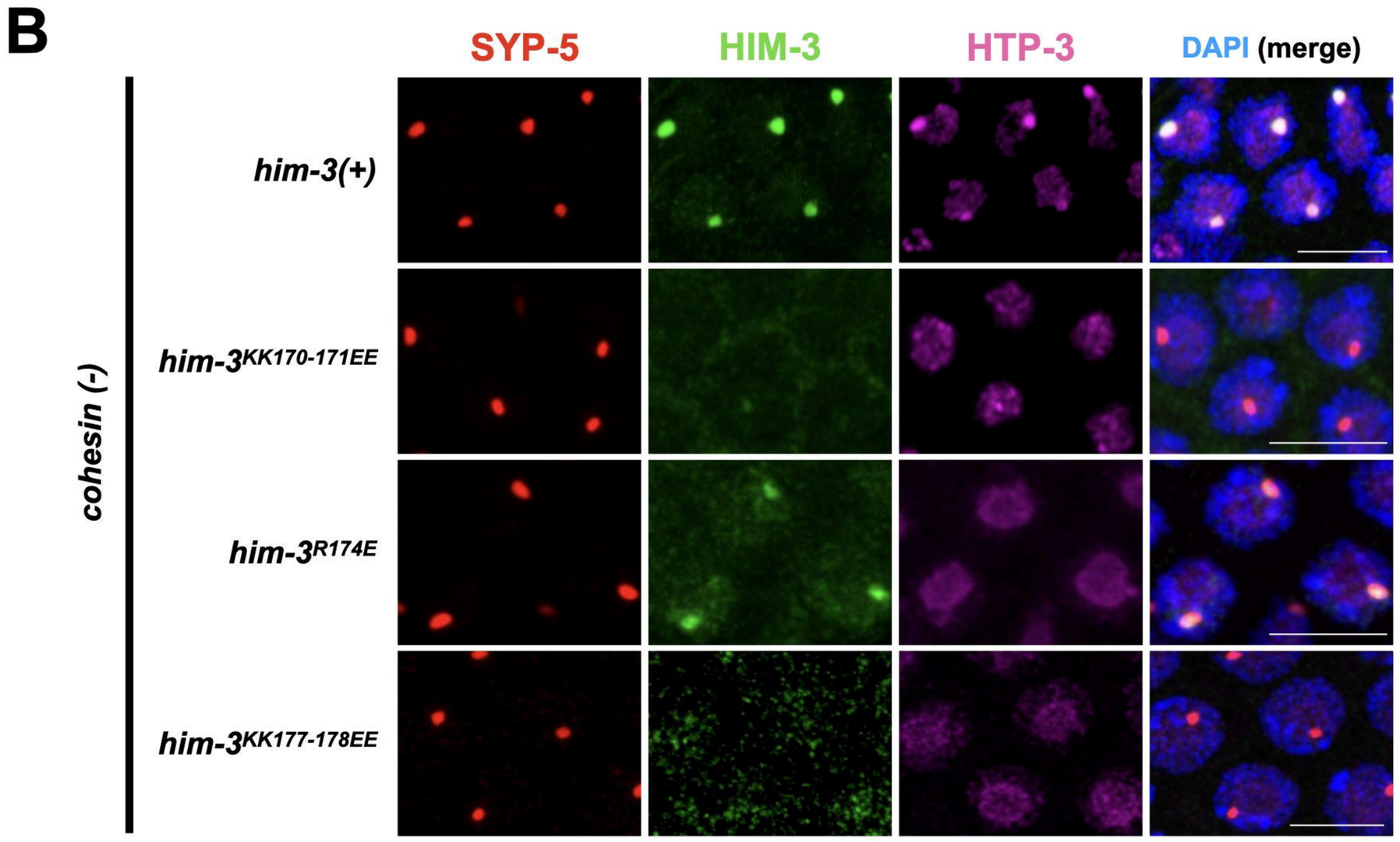

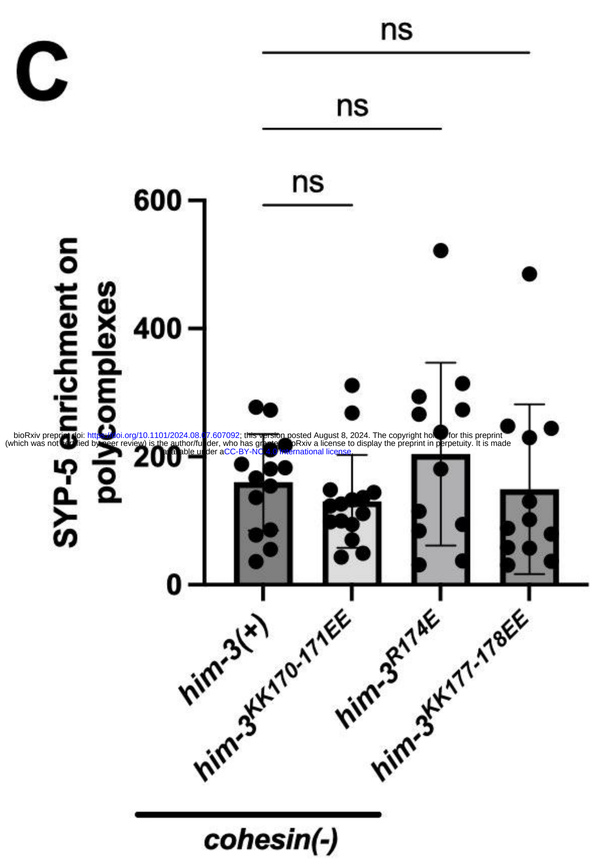

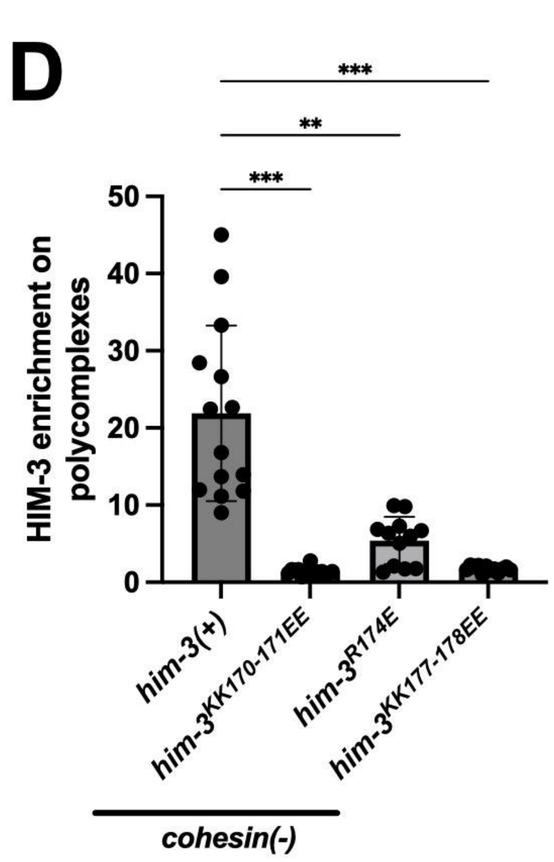

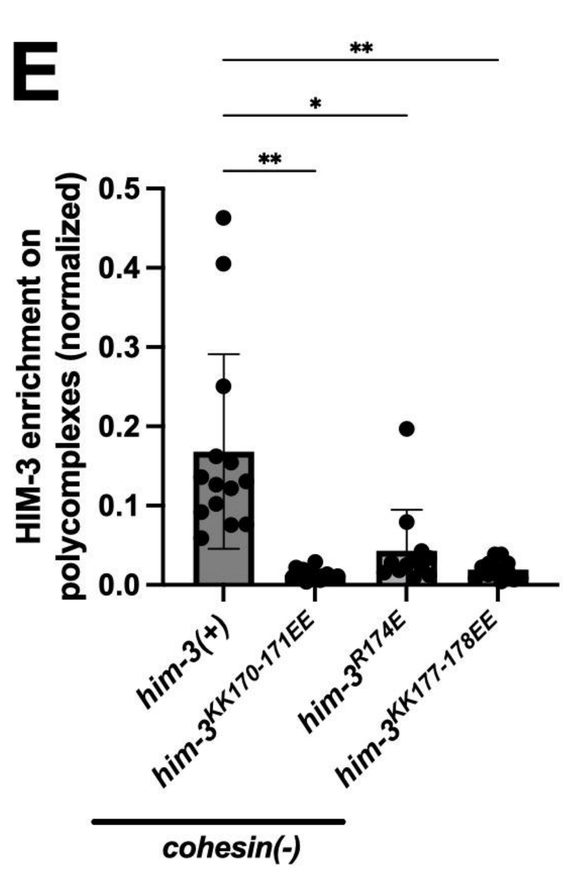

Figure 3

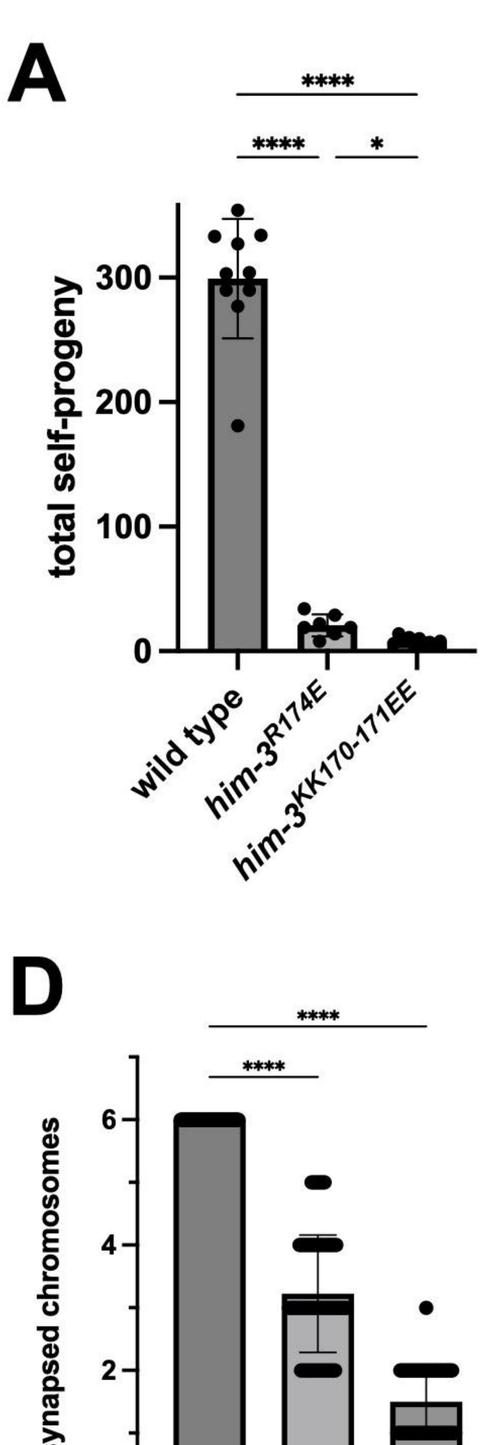

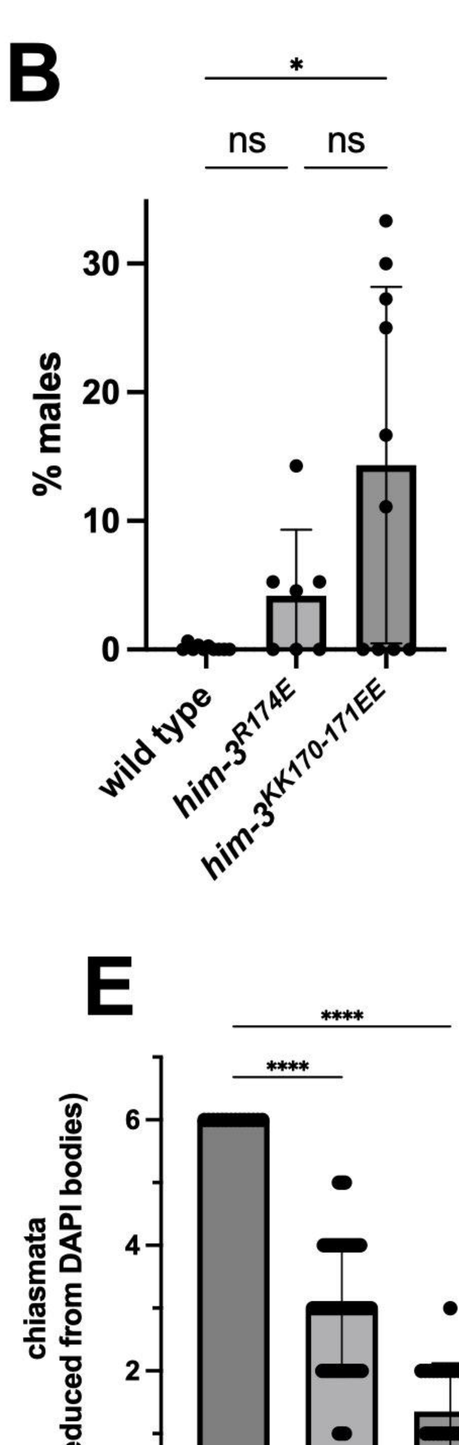

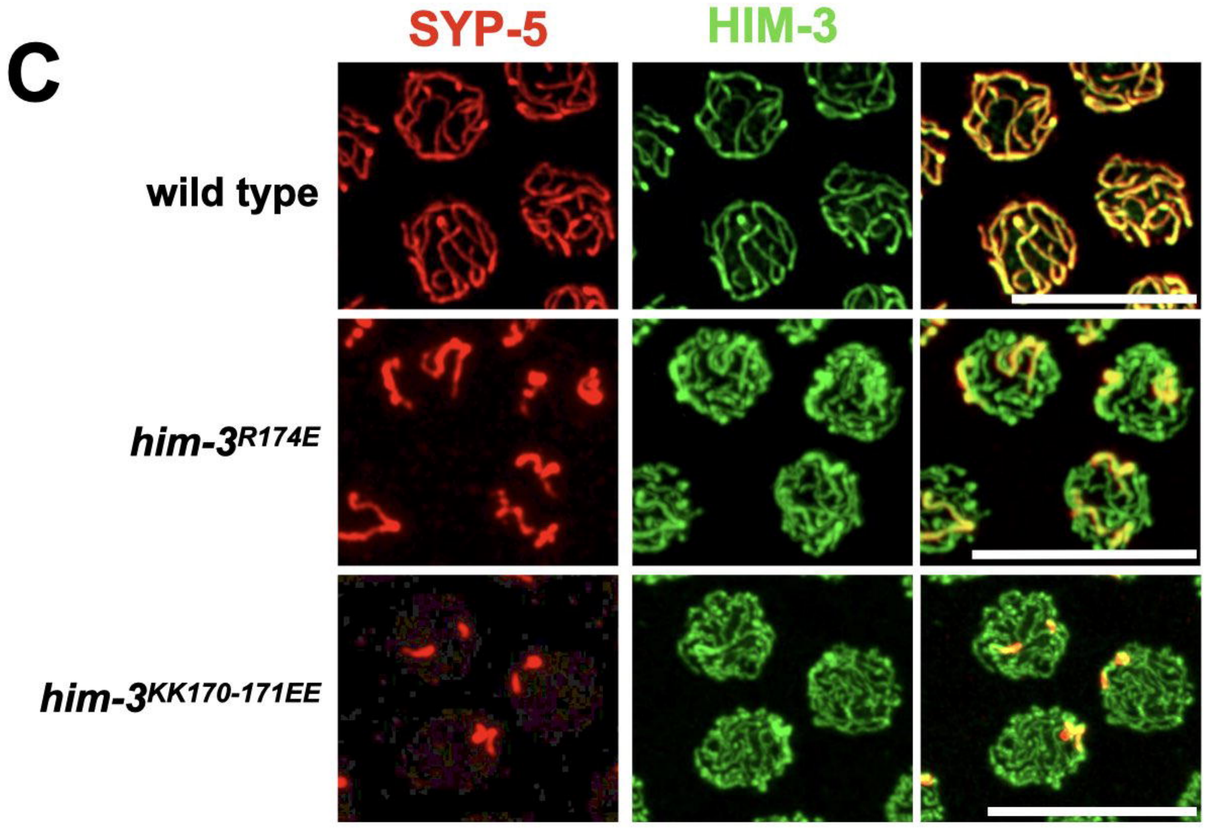

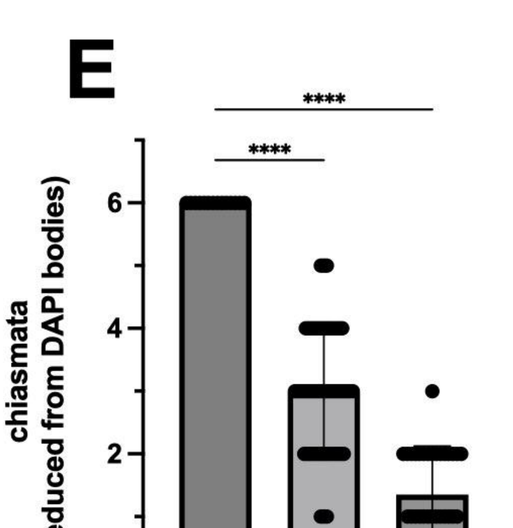

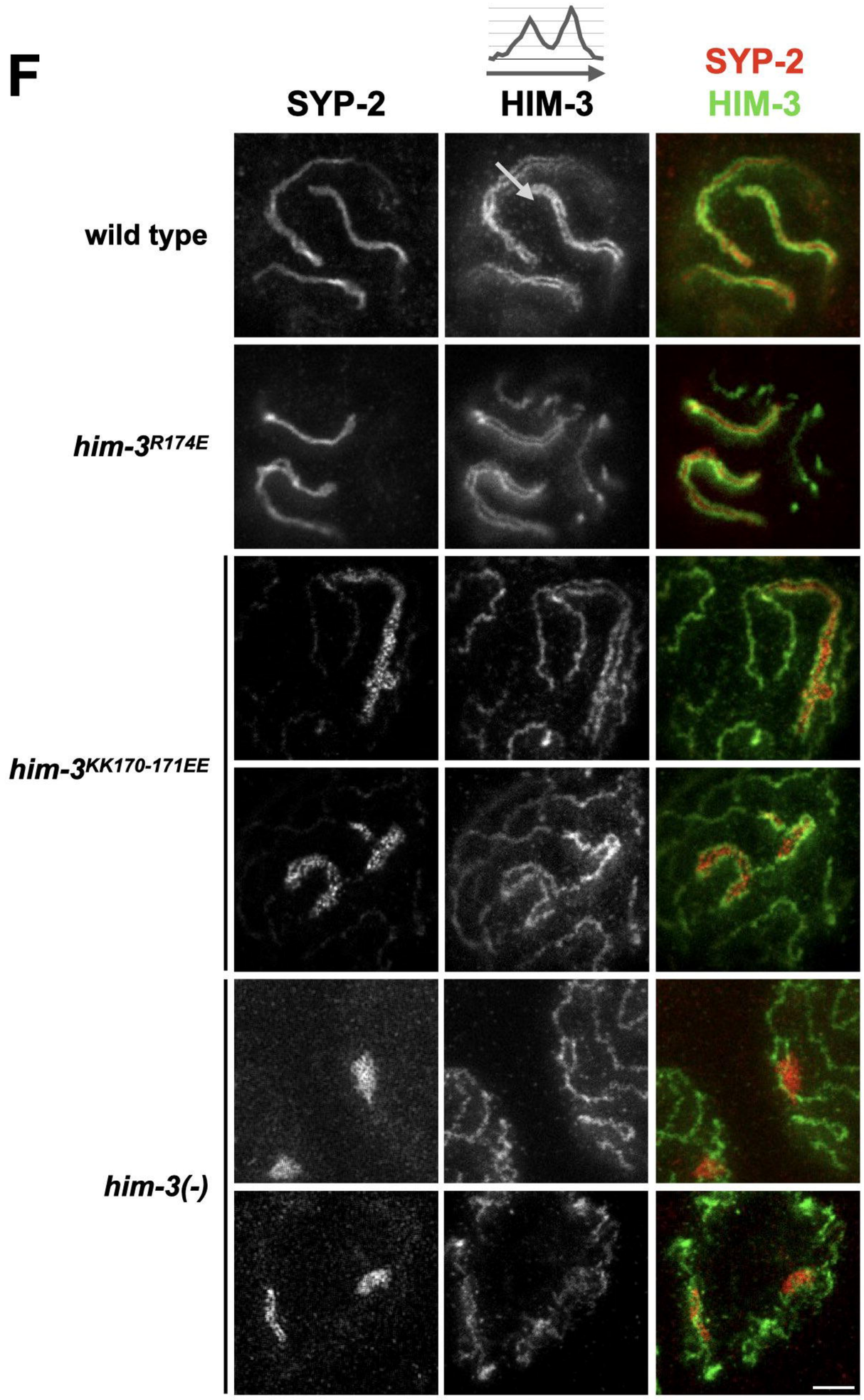

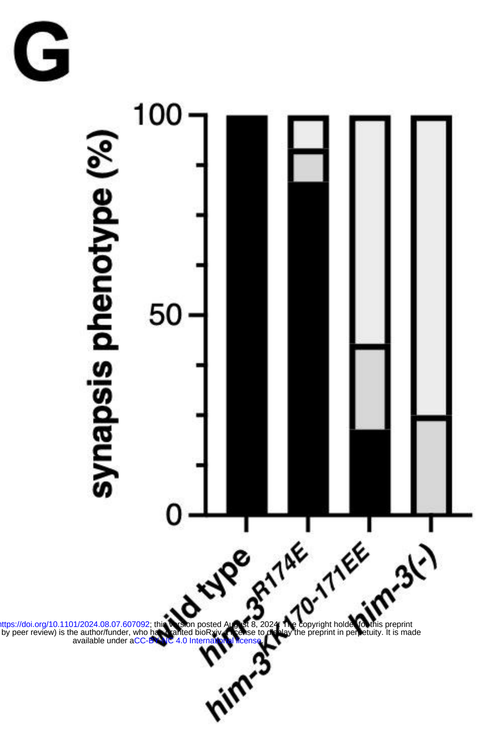

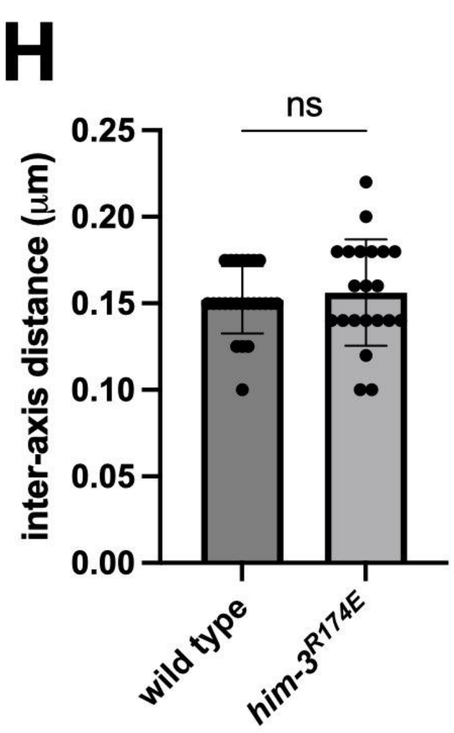

Figure 4

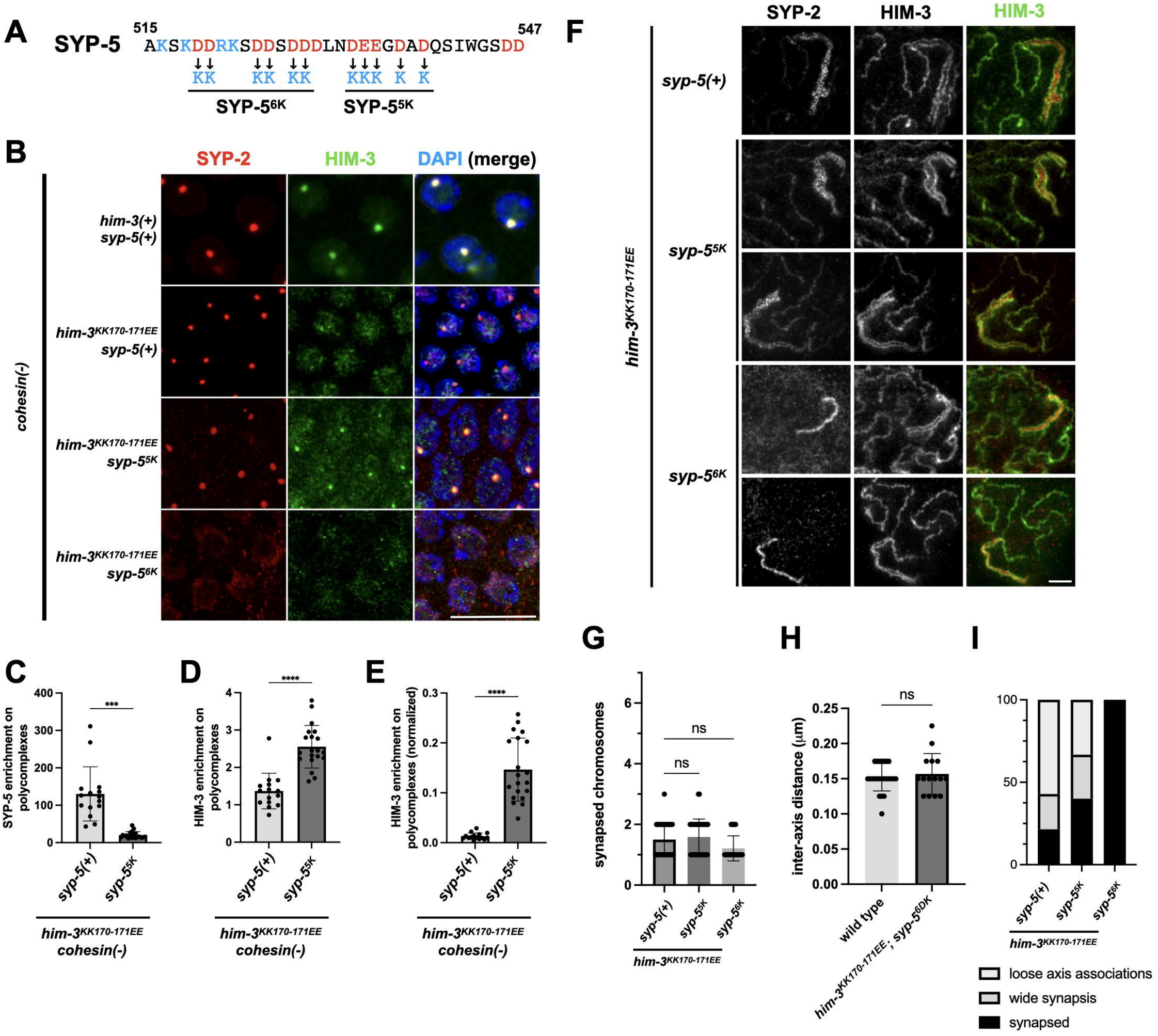

Figure 5

A

	value	reference
nuclear volume	22.5μm^3	nuclear radius = 1.75μm
nucleplasm volume	9.2μm^3	nucleolar radius = 1μm ~50% chromatin-occupied
axis length	72μm	12 chromosomes chromosome length = 6μm
SC-CR length	36μm	6 chromosome pairs
SC-CR width	100nm	(Goldstein and Slaton, 1982)
'ladder rungs' spacing	24.2nm	Panel B
SC-CR thickness	35nm	(Köhler et al., 2017, 2020)
total chromatin loop number	1,375	(Woglar et al., 2020) genome size: 220 Mb loop size: 160 kb
total HIM-3 molecules	11,000	(Woglar et al., 2020) HIM-3 molecules per loop: 8
total SYP-3 molecules	9,200	Panel C
chromosome-associated SYP-3	82%	Panel D
polycomplex volume	0.05μm^3	Panel E
SC-CR volume	0.1μm^3	6x6μmx100nmx35nm

B

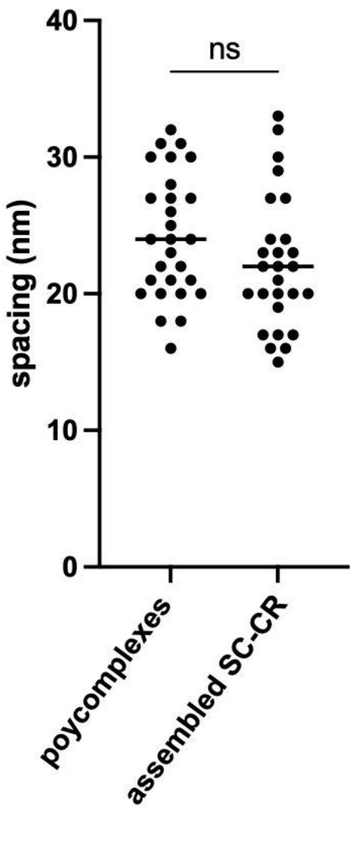

C

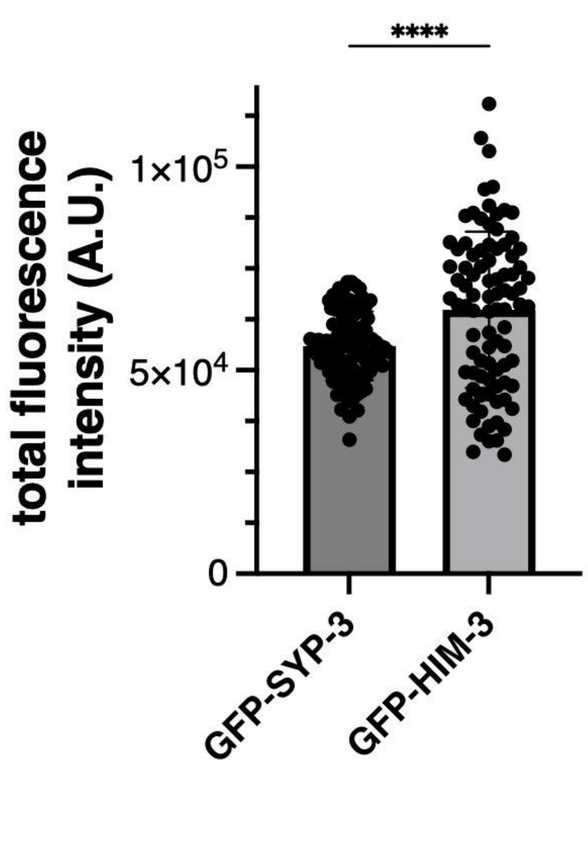

D

E

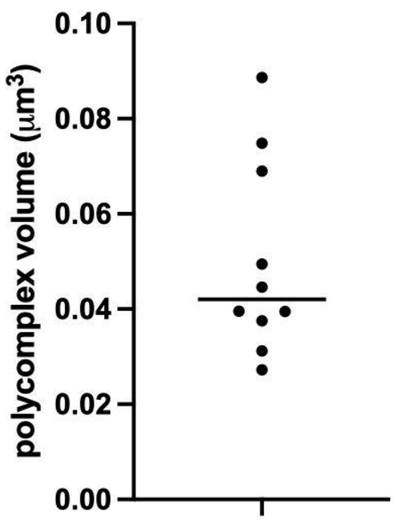

Figure 6

A

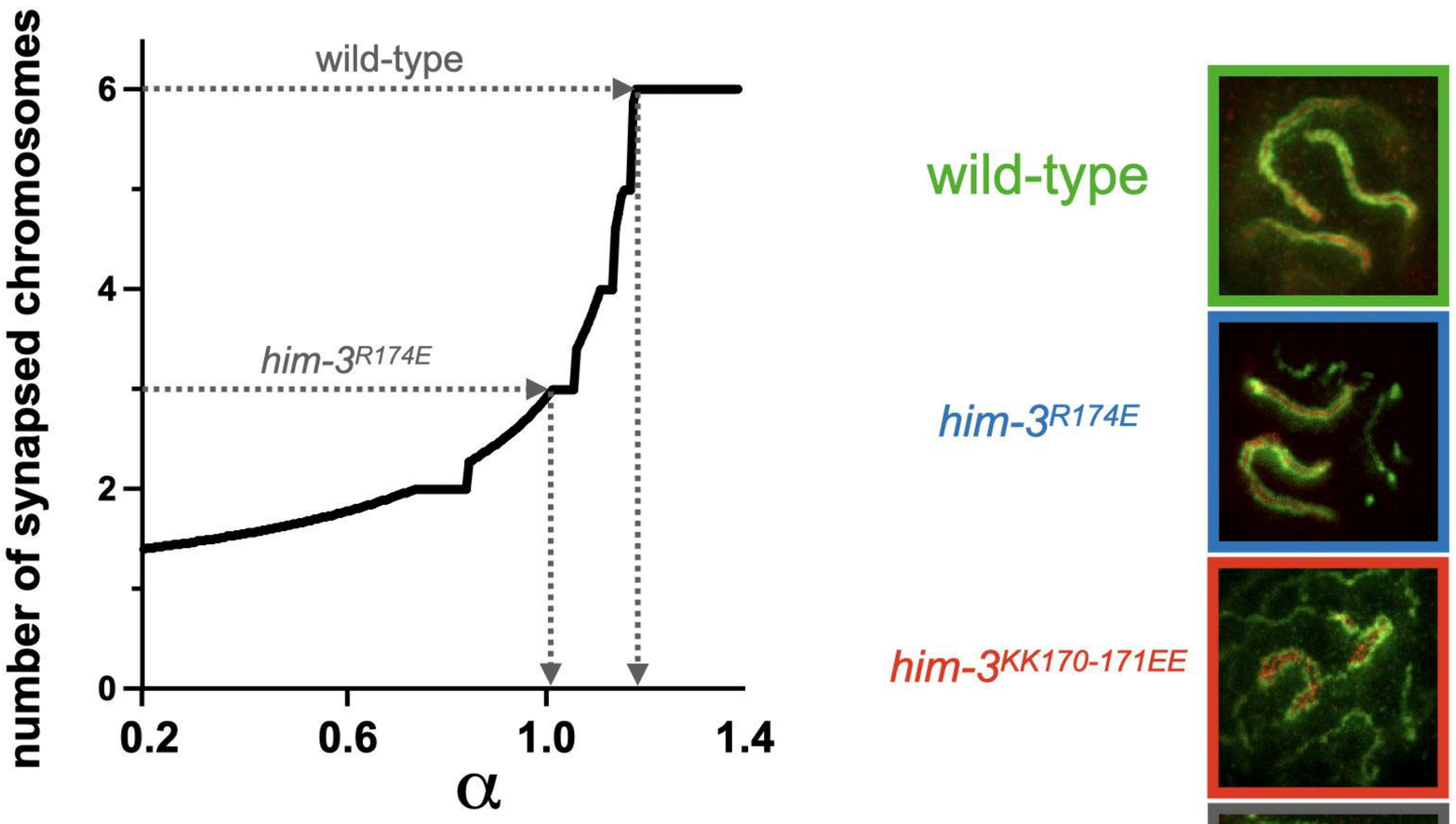

B